

1 **Relative importance of the mechanisms triggering the Eurasian** 2 **ice sheet deglaciation in the GRISLI2.0 ice sheet model**

3
4 **Victor van Aalderen¹, Sylvie Charbit¹, Christophe Dumas¹, and Aurélien Quiquet¹**

5 ¹Laboratoire des Sciences du Climat et de l'Environnement, LSCE/IPSL, CEA-CNRS-UVSQ, Université Paris-
6 Saclay, 91191 Gif-sur-Yvette cedex, France

7 **Corresponding author:** Victor van Aalderen (victor.van-aalderen@lsce.ipsl.fr)

8 **Abstract**

9 The last deglaciation (21000 to 8000 years BP) of the Eurasian ice sheet (EIS), is thought to have been responsible
10 for a sea level rise of about 20 meters. While many studies have examined the timing and rate of the EIS retreat
11 during this period, many questions remain about the key processes that triggered the EIS deglaciation 21,000 years
12 ago. Due to its large marine-based parts in the Barents-Kara and British Isles sectors, ~~EISBKIS~~ is often considered
13 as a potential analog of the current West Antarctic ice sheet (WAIS). Identifying the mechanisms that drove the
14 EIS evolution might provide a better understanding of the processes at play in the West Antarctic destabilization.
15 To investigate the relative impact of key drivers on the EIS destabilization we used the three-dimensional ice sheet
16 model GRISLI (version 2.0) forced by climatic fields from five PMIP3/PMIP4 LGM simulations. In this study,
17 we performed sensitivity experiments to test the response of the simulated Eurasian ice sheets to surface climate,
18 oceanic temperatures (and thus basal melting under floating ice tongues) and sea level perturbations. Our results
19 highlight that the EIS retreat simulated with the GRISLI model is primarily triggered by atmospheric warming.
20 Increased atmospheric temperatures further amplify the sensitivity of the ice sheets to sub-shelf melting. These
21 results contradict those of previous modelling studies mentioning the central role of basal melting on the
22 deglaciation of the marine-based Barents-Kara ice sheet. However, we argue that the differences with previous
23 works are mainly related to differences in the methodology followed to generate the initial LGM ice sheet. ~~We~~
24 ~~conclude that being primarily sensitive to the atmospheric forcing, the Eurasian ice sheet cannot be considered as~~
25 ~~a direct analogue of the present day West Antarctic ice sheet.~~ Due to the strong sensitivity of EIS to the atmospheric
26 forcing highlighted with the GRISLI model and the limited extent of the confined ice shelves during the LGM, we
27 conclude by questioning the analogy between EIS and the current WAIS. However, because of the expected rise
28 in atmospheric temperatures, risk of hydrofracturing is increasing and could ultimately put the WAIS in a
29 configuration similar to the ~~paspast~~ Eurasian ice sheet.

35 1 Introduction

36 During the last glacial maximum (LGM, 26-19 ka), the Eurasian ice complex was formed by the coalescence of
37 three distinct ice sheets covering the British Isles, Fennoscandia and the Barents and Kara Seas. While the
38 Fennoscandian ice sheet (FIS) was mostly grounded on the bedrock, the British Isles (BIIS) and Barents-Kara
39 (BKIS) were mostly lying below sea level.

40 The Eurasian ice sheet (EIS) was influenced by various climate regimes with large differences between the western
41 and eastern edges. Due to heat and moisture sources from the North Atlantic current, the British Isles and western
42 Scandinavia were dominated by relatively warm and wet conditions contrasting with the more continental and
43 drier climate in the eastern part of the EIS (Tierney et al., 2020). These various climatic influences prevailing over
44 the three different ice sheets forming the Eurasian ice complex, may have resulted in different responses to
45 variations in atmospheric and oceanic conditions. Over the last decade an active field of research has developed to
46 identify the mechanisms behind the retreat of the Eurasian ice sheet during the last deglaciation, although no clear
47 consensus has yet been reached. According to the recent study of Sejrup et al. (2022) the onset of the northern
48 hemisphere deglaciation was primarily triggered by summer ablation resulting from increased summer insolation
49 at 65 °N, and thus by changes in surface mass balance (SMB), defined as the difference between snow/ice
50 accumulation and ablation.

51 On the other hand, studies based on modeling approaches suggest that the retreat of ~~the~~ marine-based ice sheets
52 could be driven by dynamical processes triggered by the melting of ice shelves (Pattyn et al., 2018). In fact, the
53 relationship between oceanic temperatures and ice sheet mass balance has been confirmed and widely documented
54 for the present-day WAIS. In particular, it has been shown that ocean warming plays a crucial role in accelerating
55 Antarctic mass loss by enhancing basal melting and ice shelf thinning (Pritchard et al., 2012, Konrad et al., 2018,
56 Pattyn et al., 2018; Rignot et al., 2019). This process may trigger a marine ice sheet instability when the bedrock
57 is sloping towards the ice sheet interior. This instability translates into a sustained retreat of the grounding line and
58 a significant glacier acceleration (Schoof, 2012). As large parts of BIIS and BKIS are marine based, their evolution
59 could be driven by sub-shelf melting and potentially by the subsequent marine ice sheet instability. Based on the
60 analysis of benthic and planktic foraminiferal assemblages, ice-rafted debris and radiocarbon dating, Rasmussen
61 and Thomsen (2021) showed that the retreat of the ice in the Svalbard-Barents sector followed the deglacial
62 oceanic, but also atmospheric, temperature changes. Relying on a first-order thermomechanical ice sheet model
63 constrained by a variety of geomorphological, geophysical and geochronological data, Patton et al. (2017) found
64 that the BIIS receded quite quickly in response to moderate increases in surface temperature. By contrast, the BKIS
65 was rather affected by a combination of reduced precipitation and increased rates of iceberg calving. Other
66 modeling studies have attempted to simulate the dynamics of the EIS during the last glacial period and the last
67 deglaciation with the objective of better understanding the evolution of the ice sheet (Petrini et al., 2020; Alvarez-
68 Solas et al., 2019). In a way similar to what is currently observed in West Antarctica, they suggest that large EIS
69 variations are primarily due to the warming of the Atlantic Ocean leading to increased basal melting in the vicinity
70 of the grounding line (Petrini et al., 2020; Alvarez-Solas et al., 2019). However, the models on which these studies
71 are based have no specific treatment for computing ice velocities at the grounding line, making questionable their
72 representation of the grounding line migration.

73 Because of the diversity of mechanisms that may have influenced the evolution of the three Eurasian ice sheets,
74 the Eurasian ice complex is an interesting case study to investigate the different mechanisms responsible for the
75 ice sheet retreat. As both BKIS and BIIS are marine-based (Svendsen et al., 2004, Gandy et al., 2018, 2021), they
76 are likely to be more sensitive to oceanic temperature variations. Special attention can be given to BKIS because
77 it has often been considered as a potential analogue of the present-day WAIS (Gudlaugsson et al., 2017,
78 Andreassen and Winsborrow, 2009, Mercer, 1970) due to common features such as the ice volume and a bedrock
79 largely grounded below sea level with an upstream deepening (Amante et al., 2009). As a result, in-depth
80 investigations of the BKIS behavior at the LGM can help to better understand the present-day changes and future
81 evolution of West Antarctica.

82 This wide range of hypotheses regarding the different processes responsible for the EIS destabilization (i.e.
83 atmospheric climate, oceanic climate or both) confirms that there is still a lot of unknowns in the EIS dynamics
84 during the last deglaciation and that the debate is not closed. Progress has been made in ice sheet modeling with
85 the development of new generation models computing the full Stocks flow equations. For example, with a refined
86 model resolution near the grounding line, Gandy et al., (2018, 2021) have quantified the impact of oceanic
87 temperatures on the grounding line dynamics and investigated the potential occurrence and effect of the marine
88 ice sheet instability. However, as the computation time is considerably increased, they focus only on specific
89 sectors (i.e. North Sea) and thus do not consider the impact of the other interconnected ice sheets.

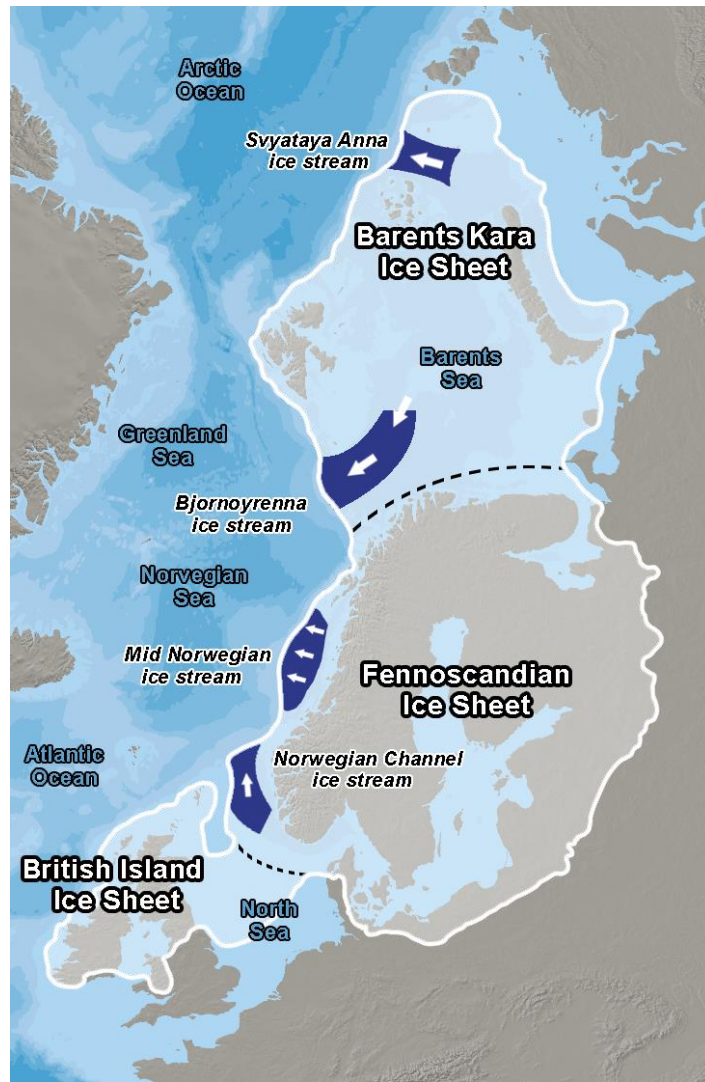
90 In this paper, we present simulations of the entire Eurasian ice complex during the LGM using the three-
91 dimensional GRISLI2.0 (GRenoble Ice Shelf and Land Ice) ice sheet model (Quiquet et al., 2018). GRISLI2.0
92 includes an explicit calculation of the ice flux at the grounding line derived from the analytical formulation
93 provided by Tsai et al. (2015), which is expected to account for the representation of the marine ice sheet instability.
94 Our ultimate objective is ~~not to identify/reproduce the key mechanisms leading to exact timing of the EIS last~~
95 ~~deglaciation— of the EIS but rather to explore the sensitivity of EIS to various perturbations using the GRISLI ice~~
96 ~~model.~~

97 Starting from its LGM geometry, we investigate the EIS sensitivity to perturbations of surface air temperature,
98 precipitation rate, basal melting, and sea level to better understand their relative contribution to the EIS
99 destabilization. In this work, the GRISLI2.0 ice sheet model was forced by a panel of ten different climates from
100 the Paleoclimate Modelling Intercomparison Project (PMIP) database (Abe-Ouchi et al., 2015; Kageyama et al.,
101 2021).

102 The paper is organized as follows. Section 2 provides a description of the basic equations of the GRISLI2.0 ice
103 sheet model. It also includes a presentation of the climate forcing and the experimental setup of the LGM and
104 sensitivity experiments. Section 3 compares our different reconstructions of the EIS at the LGM. The results of
105 the sensitivity experiments are presented in section 4 and discussed in section 5. Concluding remarks are given in
106 section 6.

107

108



109

110 **Figure 1:** Map of the Eurasian Ice Sheet at the LGM. The white line is the most credible ice extent of the Eurasian
 111 ice sheet at the LGM according to the DATED-1 compilation (Hughes et al., 2016). Dark blue shaded areas
 112 correspond to the location of the main ice streams (Dowdeswell et al., 2016; Stokes and Clark, 2001), and dotted
 113 black lines are delimitations between the Fennoscandian, the Barents-Kara, and the British Isles ice sheets.

114 **2. Model description and experimental set-up**

115 **2.1 The GRISLI ice sheet model**

116 In this study, we use the 3D thermomechanical ice sheet model GRISLI2.0 (referred hereafter to as GRISLI) run
 117 on a Cartesian grid with a horizontal resolution of 20 km x 20 km, corresponding to 177 x 257 grid points.

118 This ice sheet model was initially built to study the Antarctic ice sheet behavior during glacial-interglacial cycles
 119 (Ritz et al. 2001). It was then adapted to the Northern Hemisphere ice sheets (e.g. Peyaud et al., 2007) and tested
 120 under various climatic conditions (Ladant et al., 2014, Le clec'h et al. 2019, Colleoni et al., 2014, Beghin et al.
 121 2014). GRISLI also took part in the Ice Sheet Model Intercomparison Project (ISMIP6) (Goelzer et al.; 2020,
 122 Seroussi et al., 2020, Quiquet and Dumas, 2021a, 2021b) to investigate future sea level changes (Nowicki et al.
 123 2020). A full description of GRISLI can be found in Quiquet et al. (2018). Here, we only remind the basic
 124 principles of the model. The main modification in this new version of GRISLI compared to previous ones (Ritz et

125 al., 2001; Peyaud et al., 2007) is the implementation of analytical formulations of the flux at the grounding line
126 leading to a better representation of the grounding line migration.

127 The evolution of the ice sheet geometry depends on the ice sheet surface mass balance, ice dynamics and isostatic
128 adjustment. Assuming that ice is an incompressible material, changes in ice thickness with time are given by the
129 mass balance equation:

$$130 \quad \frac{dH}{dt} = SMB - B_{melt} - \nabla(UH) \quad (1)$$

131 with H being the local ice thickness, SMB the surface mass balance, ~~B_{melt}~~ B_{melt} the basal melting in grounded
132 ice areas and under the ice shelves, U the vertical average velocity, and $\nabla(UH)$ the ice flux divergence.

133 The ice velocity is calculated from the sum of the shallow ice approximation (SIA) and the shallow shelf
134 approximation (SSA) components (Winkelmann et al., 2011). Both approximations take advantage of the small
135 aspect ratio of the ice sheets (Hutter, 1983). The SIA assumes that the longitudinal shear stresses can be neglected
136 compared to the vertical shear stresses and holds for all ice sheet regions where the gravity-driven flow induces a
137 slow motion of the ice (Hutter, 1983). Conversely, the SSA neglects the vertical shear stresses compared to the
138 longitudinal shear stresses, which is generally valid for floating ice shelves (MacAyeal, 1989) and to some extent
139 for fast-flowing ice streams. As a result, the total ice sheet domain can be separated into three regions: floating ice
140 shelves where the ice velocity is computed with the SSA, cold-base areas governed by the SIA, and finally, the
141 temperate-base grounded ice, where the ice velocity is computed as the sum of the SIA and SSA components.

142 The basal friction for the temperate base areas is assumed to follow a linear friction law:

$$143 \quad \tau_b = -\beta U_b \quad (2)$$

144 where τ_b is the basal shear stress, U_b the basal velocity and β the basal drag coefficient. The basal drag coefficient
145 depends on the effective water pressure (N), i.e. the difference between water pressure and ice pressure, and on an
146 internal constant parameter ($C_f = 1.5 \cdot 10^{-6} \text{ m yr}^{-1}$):

$$147 \quad \beta = C_f N \quad (3)$$

148 The effective pressure N depends on the groundwater hydrology which is calculated according to Darcy's law
149 (Quiquet et al., 2018).

150 At the base of the grounded ice sheet, the basal temperature is also critically dependent on the geothermal heat
151 flux which is given here by the distribution of Shapiro and Ritzwoller (2004).

152 To simulate artificially the effect of ice anisotropy on the ice velocity, most ice sheet models use an enhancement
153 factor in the ~~nonlinear~~ non-linear viscous flow law that relates deformation rates and stresses with values generally
154 ranging between 1 and 5. In GRISLI, two enhancement factors are considered (E_{SIA} and E_{SSA}). E_{SIA} is applied to
155 the SIA component of the velocity to increase ($E_{SIA} > 1$) the deformation induced by vertical shearing. Conversely
156 E_{SSA} is applied to the SSA component of the velocity to reduce ($E_{SSA} < 1$) the deformation due to longitudinal
157 stresses. The model parameters used in this study are the same as those used in Quiquet et al. (2021c) with the
158 exception of E_{SIA} and C_f fixed respectively to 5 (instead of 1.8) and $1.5 \cdot 10^{-6} \text{ m yr}^{-1}$ (instead of $1.5 \cdot 10^{-3} \text{ m yr}^{-1}$).

159 Those parameters have been chosen for a better match between the simulated EIS ice volume at the LGM and the
 160 geologically-constrained reconstructions (see Section 2.3).

161 The horizontal resolution used in this study is too coarse to simulate explicitly the grounding line migration
 162 (Durand et al., 2009). To circumvent this drawback, we use the analytical formulation from Tsai et al. (2015), in
 163 which the ice flux at the grounding line is computed as a function of the ice thickness and a backforce coefficient
 164 accounting for the buttressing effect of the ice shelves. In this way, a flow at the grounding line can be simulated
 165 with a lower resolution allowing time saving in the simulations. Technical details on this implementation in the
 166 GRISLI model are given in Quiquet et al. (2018).

167 At the ice shelf front, calving is computed using a simple ice thickness criterion by prescribing a minimal ice
 168 thickness set to 250 m below which ice is calved.

169 In the GRISLI model, the isostatic response to ice load is handled by an Elastic-Lithosphere-Relaxed-
 170 Asthenosphere (ELRA) model (Le Meur and Huybrechts, 1996). The relaxation time of the lithosphere is set to
 171 3000 years.

172 **2.2 Climate forcing**

173 We forced GRISLI with the absolute climatic fields from general circulation model (GCM) outputs of the
 174 PMIP3/PMIP4 database (Kageyama et al., 2021). All the GCMs for which LGM simulations were available at the
 175 time of writing the manuscript have been selected (see Table 1).

176 **Table 1:** PMIP3 and PMIP4 models used to force GRISLI. The fourth column indicates the choice of the ice sheet
 177 boundary condition at the LGM for each GCM simulation. ice sheet reconstructions used as a boundary condition
 178 of the GCM simulations at the LGM.

<u>model</u>	<u>References</u>	<u>PMIP/CMIP</u>	<u>Boundary condition</u>
<u>MPI-ESM-P</u>	<u>Adloff et al. (2018)</u>	<u>CMIP5 PMIP3</u>	<u>PMIP3 ice sheet</u>
<u>MRI-CGM3</u>	<u>Yukimoto S et al. (2012)</u>	<u>CMIP5 PMIP3</u>	<u>PMIP3 ice sheet</u>
<u>MIROC-ESM</u>	<u>Sueyoshi et al. (2013)</u>	<u>CMIP5 PMIP3</u>	<u>PMIP3 ice sheet</u>
<u>CNRM-CM5</u>	<u>Voltaire et al. (2013)</u>	<u>CMIP5 PMIP3</u>	<u>PMIP3 ice sheet</u>
<u>GISS-E2-R</u>	<u>Ullman et al. (2014)</u>	<u>CMIP5 PMIP3</u>	<u>PMIP3 ice sheet</u>
<u>FGOALS-g2</u>	<u>Zheng and Yu (2014)</u>	<u>CMIP5 PMIP3</u>	<u>PMIP3 ice sheet</u>
<u>IPSL-CM5A-LR</u>	<u>Dufresne et al. (2013)</u>	<u>CMIP5 PMIP3</u>	<u>PMIP3 ice sheet</u>
<u>IPSL-CM5A2</u>	<u>Sepulchre et al. (2020)</u>	<u>CMIP6 PMIP4</u>	<u>ICE-6G_C</u>
<u>MIROC-ES2L</u>	<u>Hajima et al. (2020)</u>	<u>CMIP6 PMIP4</u>	<u>ICE-6G_C</u>
<u>MPI-ESM1.2</u>	<u>Mauritsen et al. (2019)</u>	<u>CMIP6 PMIP4</u>	<u>ICE-6G_C</u>

179
 180
 181 Monthly surface air temperatures and solid monthly precipitation are used to compute the surface mass balance
 182 defined as the difference between snow/ice accumulation and ablation. Ablation is calculated using a positive
 183 degree-day (PDD) method following the formulation of Tarasov and Peltier (2002), where the degree-day factors,

184 C_{ice} and C_{snow} depend on the mean July surface air temperature. Snow accumulation is calculated from the total
 185 precipitation (rain and snow), considering only months where monthly temperatures are under the melting point.

186 Due to the differences between GCM and GRISLI resolutions, the GCM outputs are bi-linearly interpolated onto
 187 the ice sheet model grid. In addition, to account for orography differences between GRISLI and the GCMs, the
 188 surface air temperatures of the GCMs are corrected using a constant vertical temperature gradient $\lambda = 7 \text{ }^\circ\text{C km}^{-1}$:

$$189 \quad T(t)_{GRISLI} = T_{GCM}^{LGM} - \lambda(S(t) - S_{GCM}^{LGM}) \quad (4)$$

190 where $T(t)_{GRISLI}$ is the time-dependent surface air temperature at the surface elevation $S(t)$ simulated by the ice
 191 sheet model, and T_{GCM}^{LGM} and S_{GCM}^{LGM} are the LGM surface air temperature and orography computed by the GCMs.
 192 This temperature correction induces a change in precipitation which is computed following the Clausius-Clapeyron
 193 formulation for an ideal gas:

$$194 \quad pr(t)_{GRISLI} = pr_{GCM}^{LGM} * \exp(\omega * (T(t)_{GRISLI} - T_{GCM}^{LGM})) \quad (5)$$

195 where $pr(t)_{GRISLI}$ is the precipitation calculated by GRISLI at each time step and pr_{GCM}^{LGM} is the LGM precipitation
 196 computed by the GCM and interpolated on the GRISLI grid. ω is the precipitation ratio to temperature change and
 197 is fixed to $0.11 \text{ }^\circ\text{C}^{-1}$ (Quiquet et al., 2013).

198 Following DeConto and Pollard (2012), the sub-shelf melt rate (OM) is computed using ocean temperature and
 199 salinity:

$$200 \quad OM = K_t \frac{\rho_w C_w}{\rho_i L_f} |T_o - T_f| (T_o - T_f) \quad (6)$$

201 where K_t is called the transfer factor and is set to $7 \text{ m yr}^{-1} \text{ }^\circ\text{C}^{-1}$ in the baseline experiments as in DeConto and
 202 Pollard (2012), ρ_w the ocean water density, ρ_i ice density, L_f the latent heat of ice fusion, C_w the specific heat of
 203 ocean water and T_o is the local ocean temperature. T_f is the local freezing point temperature, depending on the
 204 ocean salinity (S) and computed by the Beckmann and Goosse (2003) parameterization:

$$205 \quad T_f = 0.0939^\circ\text{C} - S \times 0.057^\circ\text{C} + z \times 7.6410^{-4}^\circ\text{C} \quad (7)$$

206 where z is the ocean depth.

207 A difficulty related to the oceanic forcing fields is that the GCMs do not provide any oceanic information outside
 208 their land-sea mask and under the ice shelves. To fill these gaps, we performed a classical near neighbour horizontal
 209 extrapolation of temperature and salinity except that we perform this extrapolation within 10 sectors
 210 independently. These sectors roughly correspond to drainage basins (Fig. S1). The definition of these basins is
 211 based on bedrock topographic features and LGM ice elevation and is somehow comparable to the approach
 212 followed by Zwally et al. (2015) for Antarctica. The horizontal extrapolation is performed for each individual
 213 vertical layer, without any vertical interpolation. This extrapolation method provides information on temperature
 214 and salinity within the entire ice shelf cavity for each vertical level of the GCMs. These temperature and salinity
 215 fields are then used to compute the sub-shelf melt rate (Eq. 6), using a linear vertical interpolation between the two
 216 oceanic layers bounding the ice shelf depth. The only exception is when the PMIP3/PMIP4 simulations do not

217 provide data in a given sector. In this case, a constant and homogeneous basal melting value of 0.1 m yr^{-1} is
 218 prescribed. This mainly occurs in the continental southern flanks of the Eurasian ice sheet.

219 In GRISLI, each grid point can either be a floating or a grounded ice point. To account for the fact that the sub-
 220 shelf melt rate is higher in the vicinity of the grounded line (Beckmann and Goose, 2003) and due to the coarse
 221 resolution of the model, we apply a fraction of the ~~neighbouring~~neighboring floating sub-shelf melt rate to the last
 222 grounded point as in De Conto and Pollard (2012). This approach allows to take the potential influence of the
 223 ocean into account.

224 The main parameters and parameterizations used in this study are shown in Table 2 and Table 3.

225 Table 2: Model parameters of the GRISLI ice-sheet model used in this study

<u>Parameters</u>	<u>Identifier name</u>	<u>Value</u>
<u>Enhancement factor (SIA)</u>	E_{SIA}	<u>5</u>
<u>Enhancement factor (SSA)</u>	E_{SSA}	<u>1</u>
<u>Atmospheric temperature lapse rate</u>	λ	<u>$7 \text{ }^\circ\text{C km}^{-1}$</u>
<u>Precipitation ratio to temperature change</u>	ω	<u>$0.11 \text{ }^\circ\text{C}^{-1}$</u>
<u>Oceanic heat transfer factor</u>	K_t	<u>$7 \text{ m yr}^{-1} \text{ }^\circ\text{C}^{-1}$</u>
<u>Thickness threshold for the calving criterion</u>	H_{cut}	<u>250 m</u>
<u>Relaxation time of the asthenosphere</u>	R_{time}	<u>3000 years</u>
<u>Basal drag parameter</u>	C_f	<u>$1.5 \cdot 10^{-6} \text{ m yr}^{-1}$</u>

226

227 Table 3: Parameterizations of the GRISLI ice-sheet model used in this study

<u>Parameterizations</u>	<u>References</u>
<u>Positive degree-days</u>	<u>Tarasov and Peltier (2002)</u>
<u>Basal melting below ice shelves</u>	<u>Deconto and Pollard (2012)</u>
<u>Flux at the grounding line</u>	<u>Tsai et al. (2015)</u>
<u>Basal friction law</u>	<u>Linear law / Weertman (1957)</u>

228

229 ~~Table 1: PMIP3 and PMIP4 models used to force GRISLI. The fourth column indicates the choice of the ice sheet
 230 boundary condition at the LGM for each GCM simulation. ice sheet reconstructions used as a boundary condition
 231 of the GCM simulations at the LGM.~~

<u>model</u>	<u>References</u>	<u>PMIP/CMIP</u>	<u>Boundary condition</u>
MPI-ESM-P	Adloff et al. (2018)	CMIP5-PMIP3	PMIP3 ice sheet
MRI-CGM3	Yukimoto S et al. (2012)	CMIP5-PMIP3	PMIP3 ice sheet
MIROC-ESM	Sueyoshi et al. (2013)	CMIP5-PMIP3	PMIP3 ice sheet
CNRM-CM5	Voldoire et al. (2013)	CMIP5-PMIP3	PMIP3 ice sheet
GISS-E2-R	Ullman et al. (2014)	CMIP5-PMIP3	PMIP3 ice sheet
FGOALS-g2	Zheng and Yu (2014)	CMIP5-PMIP3	PMIP3 ice sheet

IPSL-CM5A-LR	Dufresne et al. (2013)	CMIP5-PMIP3	PMIP3-ice-sheet
IPSL-CM5A2	Sepulchre et al. (2020)	CMIP6-PMIP4	ICE-6G-C
MIROC-ES2L	Hajima et al. (2020)	CMIP6-PMIP4	ICE-6G-C
MPI-ESM1-2	Mauritsen et al. (2019)	CMIP6-PMIP4	ICE-6G-C

232 2.3 LGM equilibrium

233 As mentioned above, the main objective of the present paper is to investigate the mechanisms responsible for the
 234 EIS retreat from its LGM configuration. To do this, a preliminary step is to build the EIS at the LGM.

235 We performed ten 100 000-~~years~~~~year~~ spin-up experiments (one for each GCM) forced by a constant LGM climate
 236 provided by the ten GCMs. Simulations start with no ice sheet and the eustatic sea level is prescribed at 120 m
 237 below the present level. The initial bedrock topography corresponds to the present-day topography from ETOPO1
 238 (Amante et al., 2009). This procedure is required to obtain internal ice sheet conditions in equilibrium with the
 239 climate forcing and to examine whether the LGM climate can build and maintain the EIS when it is used as input
 240 to the GRISLI ice sheet model. From this climate forcing ensemble, we only selected those leading to LGM ice
 241 sheets in a reasonable agreement with the most credible ice extent in the DATED-1 database (Hughes et al., 2016)
 242 and with the geologically-constrained ice thickness reconstructions, namely ICE-6G_C (Peltier et al., 2015),
 243 GLAC-1D (Briggs et al., 2014; Tarasov et al., 2012; Tarasov and Peltier, 2002), and ANU (Lambeck et al., 1995,
 244 1996, 2010).

245 2.4 Sensitivity experiments

246 To quantify the relative importance of the three main drivers (i.e., surface mass balance, sub-shelf melt rate, and
 247 sea level) of the EIS retreat, we applied time-constant perturbations on the atmospheric and oceanic GCM forcings,
 248 and we changed the prescribed sea level. The perturbed simulations are run for 10000 years. We analysed the
 249 response at year 1000 of the simulation to investigate the impacts of climate changes that may have occurred at
 250 the beginning of the deglaciation and at year 10,000 to examine the sensitivity of EIS on longer time scales.

251 In the first series of experiments (EXP1), we investigate the effect of SMB changes by increasing surface air
 252 temperatures. During the last deglaciation (21 – 8 ka), the mean annual global surface air temperature increased
 253 by $4,5^{\circ} \pm 0,9^{\circ}$ (Annan et al., 2022). In order to simulate a range of anomalies representative of the onset of the last
 254 deglaciation, we chose to apply perturbations from 1 to 5 °C to the mean annual GCM forcing fields, without
 255 accounting for related changes in precipitation (see Eq 5). The increase in precipitation in response to increased
 256 temperatures (Eq. 5) is considered in the second set of experiments (EXP2).

257 The third series of experiments (EXP3) is designed to assess the role of oceanic forcing on the EIS stability.
 258 Because the basal melting below the ice shelves depends linearly on the Kt transfer coefficient and is a quadratic
 259 function of the oceanic temperatures, we performed two sub-series of experiments by modifying either the Kt
 260 values (EXP3.1) without modifying the oceanic temperatures, or by applying perturbations to the oceanic
 261 temperatures (EXP3.2). Observations below the Antarctic ice shelves show that the basal melting rate ranges from
 262 0 to 35 m yr⁻¹ for oceanic temperatures between -2 °C and 2 °C (Holland et al., 2008). This wide range of basal
 263 melting rate values reflects the complexity of such a process that can only be partially represented with simple
 264 parameterizations (Eq. 6). The Kt coefficient is thus largely uncertain. Therefore, to investigate changes in the EIS

265 sensitivity to the amplitude of basal melting, we first use a wide range of values for this transfer coefficient, i.e.
266 between 10 and 50 m yr⁻¹°C⁻¹.

267 The mean global sea surface temperature anomaly inferred from the MARGO project (MARGO project members,
268 2009) between the Late Holocene and the LGM is 1.9 ± 1.8°C consistent with the findings (~2.7°C) of Tierney et
269 al. (2020). In the early phase of the deglaciation, the ocean warming was probably less than that of the Late
270 Holocene. Therefore, for the EXP3.2 experiments, we first apply perturbations of 0.5°C, 1.0°C, 1.5°C to the
271 oceanic temperatures (same perturbation on all vertical levels) and we fix the Kt coefficient to 7 m °C⁻¹ yr⁻¹. In the
272 transient simulation of the last deglaciation performed by Liu et al. (2009), large increases in oceanic temperatures
273 are obtained. For example, a +9°C warming is obtained in the BJR sector at 500-600 m ocean depth and almost
274 7.5°C in the SA sector at 400-500 m. To reproduce the large increase in the subsurface ocean temperature obtained
275 in Liu et al. (2009), we performed additional sensitivity experiments with perturbations of 7.5°C and 10°C applied
276 in the entire oceanic column.

277 Atmospheric and oceanic temperatures are the two main factors potentially responsible for the destabilization of
278 marine ice sheets. Thus, the fourth series of experiments (EXP4) combines surface air temperature perturbations
279 ($\Delta T = +2^\circ\text{C}$, $+3^\circ\text{C}$, and $+4^\circ\text{C}$) with basal melting rate perturbations ($K_t = 10, 15$ and $25 \text{ m yr}^{-1} \text{ }^\circ\text{C}^{-1}$).

280 ~~Finally, in~~In the fifth set of experiments (EXP5), we also explore the EIS sensitivity to sea level. Indeed, sea level
281 rise favors the retreat of the grounding line and is therefore another potential driver of the MISI. At the beginning
282 of the deglaciation, the global sea level increased by more than 10 m (Carlson and Clark, 2012) raising the global
283 sea level from -120 m to -110 m compared to the present-day eustatic sea level. This abrupt change may have
284 played an important role in the destabilisation of the ice sheet. On the other hand, Gowan et al., (2021) shows that
285 the local sea level around the EIS margin displays a significant spread at the LGM, from -70 m to -140 m,
286 compared to the present-day level and can abruptly change in response to variations in the land-ice mass
287 distribution. Consequently, to better explore the EIS sensitivity to both global mean sea level and local sea level
288 at the beginning of the last deglaciation, we apply moderate (-115 m, -110 m, and -105 m) and large (-90 m, -60 m,
289 -30 m, and 0 m) sea level perturbations with respect to the present day.

290 **3. Available ice sheet reconstructions and ice streams signature**

291 **3.1 Ice sheet geometry**

292 The DATED-1 database is based on evidence found in the existing literature and retrieved from various geological
293 materials (e.g., terrestrial plant macrofossils, foraminifera, speleothems, bones...) ~~analyzed~~analysed with a range
294 of dating methods. Based on these data, the DATED-1 compilation provides three different scenarios for the
295 maximal, minimal and most credible EIS extent. The GLAC-1D, ICE-6G_C, and ANU reconstructions are based
296 on inverse modeling approaches constrained by GPS data, relative sea level and geomorphological data.

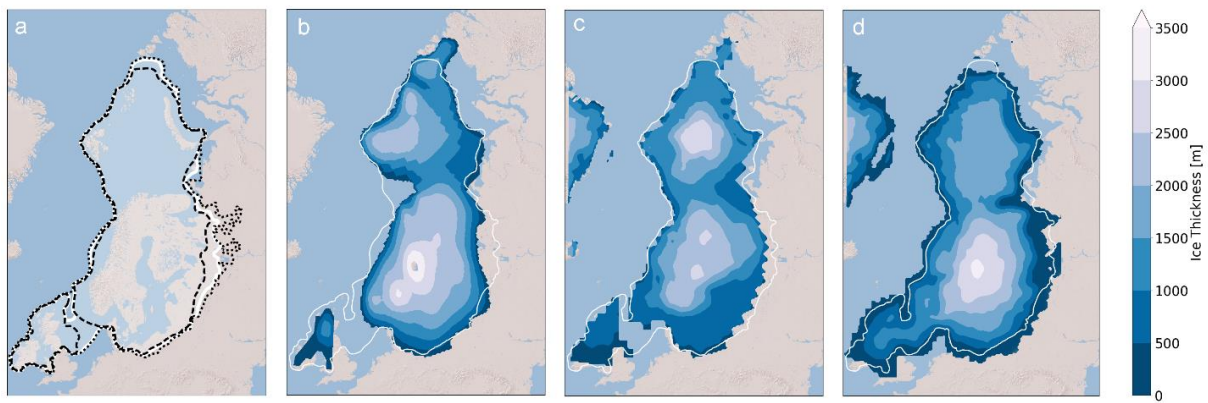
297 The main differences in the three DATED-1 scenarios at the LGM (Hughes et al., 2016) are related to the potential
298 BIIS-FIS connection (or disconnection), the southern continental limit of the FIS and the eastern limit of BKIS
299 (Fig. 2a). Only the minimum scenario suggests the absence of ice between the BIIS and FIS.

300 The GLAC-1D reconstruction agrees well with the most credible DATED-1 scenario, despite a slightly greater ice
301 extent in most of the Fennoscandian regions and a smaller extent in the Taymyr Peninsula (in the easternmost part

302 of the BKIS, Fig. 2d). This contrasts with the ANU and ICE-6G_C reconstructions whose ice limit goes beyond
303 that of the most credible DATED-1 scenario.

304 The differences between the three geologically-constrained reconstructions are due to differences in the inverse
305 methods used to estimate the ice thickness, to the geological and geomorphological data considered to infer the
306 ice extent, and to different choices regarding the Earth rheology. This translates into differences in the altitude of
307 the EIS. For example, in the ANU and GLAC-1D reconstructions, the FIS peaks at 3000-3500 m, while BKIS
308 does not exceed 2500 m (2000 m for GLAC-1D). By contrast, ICE-6G_C provides a larger ice thickness over the
309 BKIS sector (2500-3000 m) than over Fennoscandia.

310



312

312 **Figure 2:** a/ Ice sheet extent at the LGM derived from the DATED-1 compilation (Hughes et al., 2016). The
313 maximum and the minimum scenarios of the ice extent are represented by the dotted and the dashed lines
314 respectively. b/ Ice thickness at the LGM provided by the ANU reconstruction (Lambeck et al., 1995, 1996, 2010;
315 Abe-Ouchi et al., 2015). c/ Same as b/ for the ICE-6G_C reconstruction (Peltier et al., 2015). d/ Same as b/ for the
316 GLAC-1D reconstruction (Briggs et al., 2014; Tarasov et al., 2012; Tarasov and Peltier, 2002). In the four panels,
317 the white line corresponds to the most credible scenario of the ice extent at the LGM derived from the DATED-1
318 compilation (Hughes et al., 2016).

319 3.2 Ice stream signature

320 Ice streams also play a key role in ice sheet dynamics and in featuring ice sheet geometry (Pritchard et al., 2009).
321 It is therefore crucial that the dynamics of the simulated ice sheets is consistent with reconstructions. The signature
322 of ice streams can be inferred from geomorphological observations in the Barents Sea, in particular those of the
323 Bjornoyrenna (BJR) and Svyataya Anna (SA) ice streams (Fig. 1) (Polyak et al., 1997; Andreassen and
324 Winsborrow, 2009; Dowdeswell et al., 2016,2021; Szuman et al., 2021). Other geomorphological observations
325 strongly suggest the existence of paleo ice streams in the FIS, such as the Mid-Norwegian (MN) ice stream (Stokes
326 and Clark, 2001), and the Norwegian Channel (NC) ice stream between the FIS and BIIS (Sejrup et al., 1994;
327 Svendsen et al., 2015; Stokes and Clark, 2001).

328

329

330 **4. Results**

331 **4.1 LGM equilibrium**

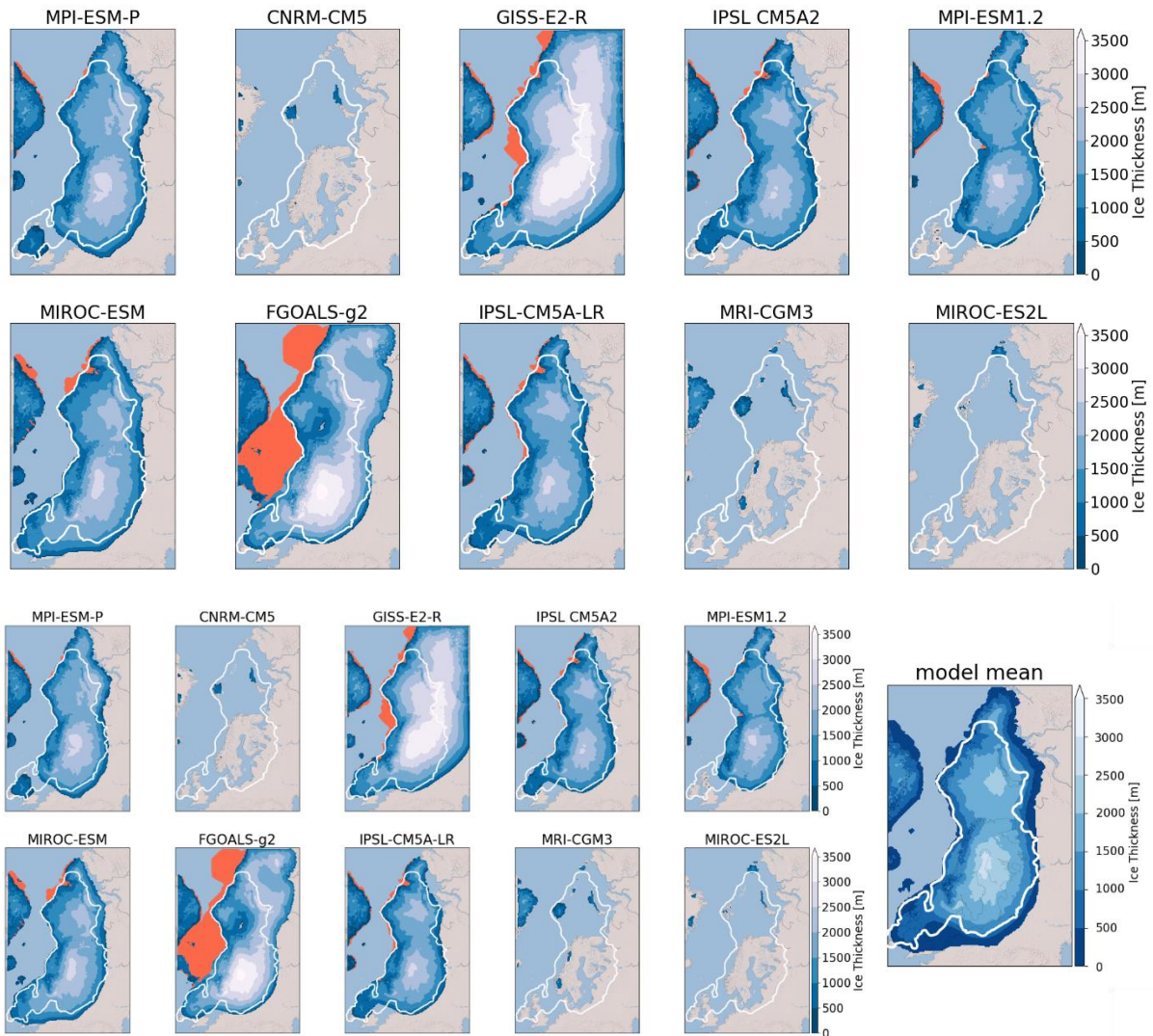
332 At the end of the 100 000-year spin-up simulations, a wide range of ice sheet geometries is obtained (Fig. 3).
333 Simulations performed with CNRM-CM5, MRI-CGM3 and MIROC-ES2L do not succeed in building an ice sheet
334 over Eurasia.

335 This is primarily explained by high positive summer surface air temperatures simulated by the three models in
336 most parts of the EIS compared to the other models, with temperature anomalies ranging between +4.7°C and
337 +11.7°C (Fig. 4). Conversely, with the GISS-E2-R and FGOALS-g2 models, significant ice thickness is built east
338 and south of BKIS because of strong negative mean summer temperatures in this area (Fig. 4).

339 Therefore, we discarded these models and only selected those (MPI-ESM-P, MIROC-ESM, IPSL-CM5A2, IPSL-
340 CM5-LR, and MPI-ESM1.2) providing ice sheet geometries in a relatively good agreement with the
341 reconstructions.

342 The five selected ice sheets do not show significant differences (Fig 3). The FIS peaks at 2500-3000 m, while the
343 BKIS is lower (2000 – 2500 m) due to a drier atmosphere compared to that overlying the Fennoscandian region
344 (Fig. 5). The simulated FIS agrees with the ICE-6G_C reconstruction despite a flatter dome simulated with MPI-
345 ESM-P, about 500 m lower compared to GLAC-1D and ANU. Conversely, the BKIS maximum altitude simulated
346 by GRISLI is underestimated compared to ICE-6G_C while it is in good agreement with the two other
347 reconstructions. The BKIS margins bordering the Greenland and Norwegian Seas and the Arctic Ocean generally
348 match with the most credible DATED-1 scenario of the ice extent. However, in the five GRISLI simulations, the
349 ice extent is too large in the eastern and southern edges compared to DATED-1.

350 The most likely cause of this mismatch is related to the imprint of the ice sheet reconstructions used as boundary
351 conditions of GCM simulations. Indeed, both the ice sheet reconstruction used for PMIP3 simulations (not shown)
352 and ICE-6G_C (Fig. 2c) used in PMIP4 runs overestimate the ice extent in the region of the Taimyr Peninsula.
353 This results in an enhanced cooling favoring the simulated ice expansion in this area. This effect can be amplified
354 by the projections of the ice sheet reconstructions on the coarser GCM grid that may produce an artificial spread
355 of the ice sheet mask, causing further a too extended cooling. Another source of disagreement between DATED-
356 1 and the simulated ice sheets can be due to the representation the jet stream and planetary waves in the coarse
357 resolution climate models, such as the PMIP models. Indeed, such large-scale atmospheric features directly impact
358 the simulated precipitation and temperatures and may cause too much precipitation or too much cooling if
359 improperly represented (Löfverström and Liakka, 2018).



360

361

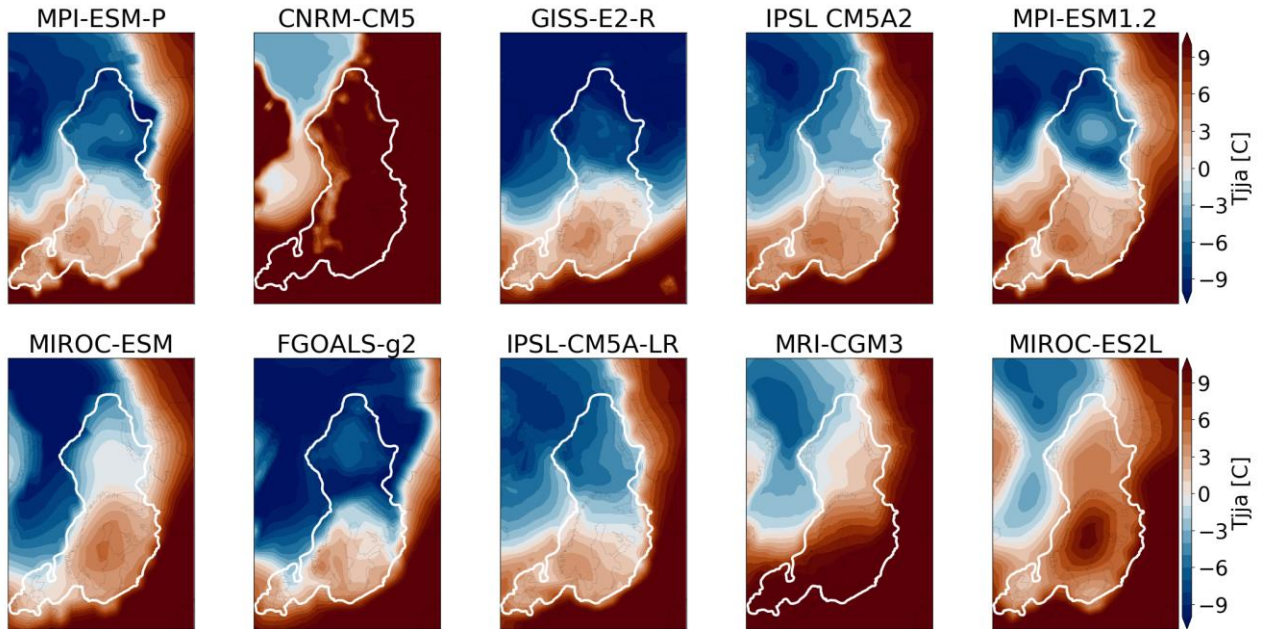
362 **Figure 3:** Ice thickness at the end of the 100 000-year simulation for the different GCMs used as forcing of the
 363 GRISLI ice sheet model. The white line is the most credible extent derived from the DATED-1 compilation and
 364 the orange shaded areas are the simulated ice shelves. The multi model mean of the five selected ice sheet is shown
 365 in the right panel.

366 For the five selected GCMs, areas with high ice velocities are simulated in the BKIS region (Fig. 6). The highest
 367 velocities are obtained for the SA, BJR, NC and MN ice streams and can exceed 1000 m yr^{-1} . In addition, the BJR
 368 ice stream shows a large extension from the center of BKIS, with velocities between 75 to 200 m yr^{-1} , to the edge
 369 of BKIS. The location of the main fast flowing areas is consistent with empirical evidence based on observations
 370 of submarine landforms (Dowdeswell et al., 2016; Stokes and Clark, 2001). It is also interesting to mention that
 371 ice velocities of similar magnitude in the present-day Antarctic and Greenland ice sheets have been revealed thanks
 372 to radar observations (Solgaard et al., 2021; Mougnot et al., 2019).

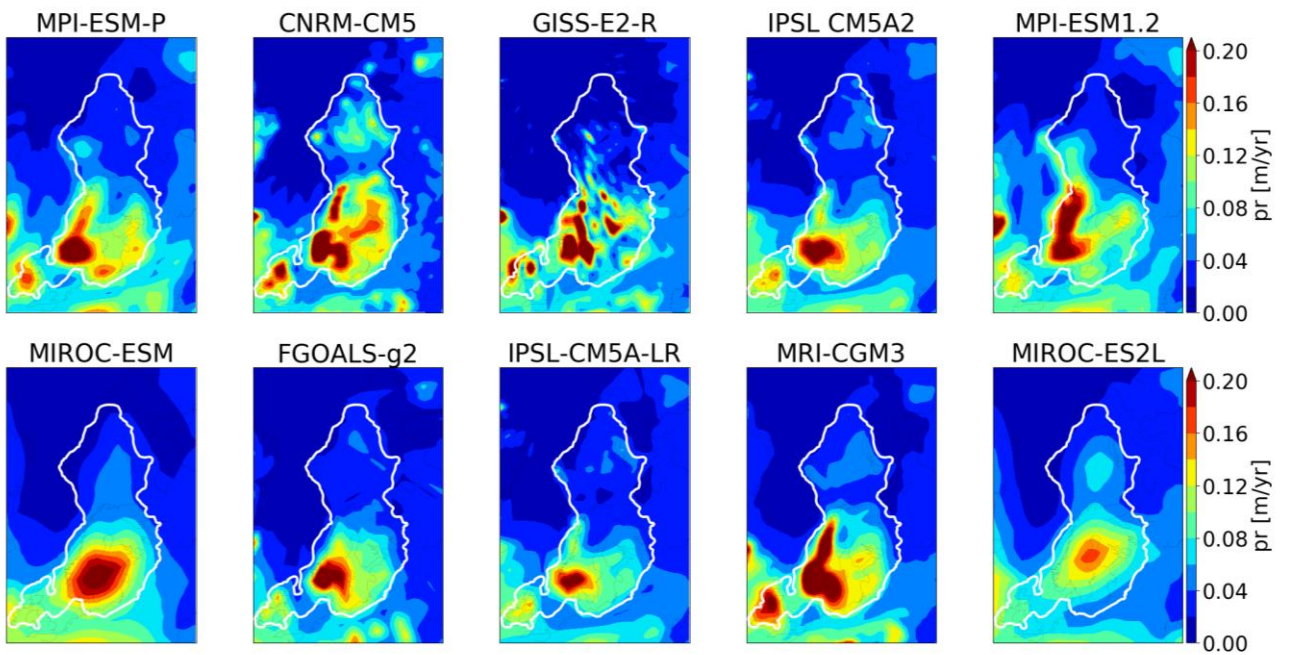
373 Overall, our five remaining simulated ice sheets show a reasonable agreement with the different reconstructions
 374 constrained by geological and geomorphological observations, both in terms of ice extent and ice thickness as well
 375 as dynamical characteristics. The observed differences with the reconstructions remain within the range of

376 uncertainties, which is itself illustrated by the differences between the three reconstructions GLAC-1D, ANU and
377 ICE-6G_C and by the three ice extent scenarios from the DATED-1 compilation.

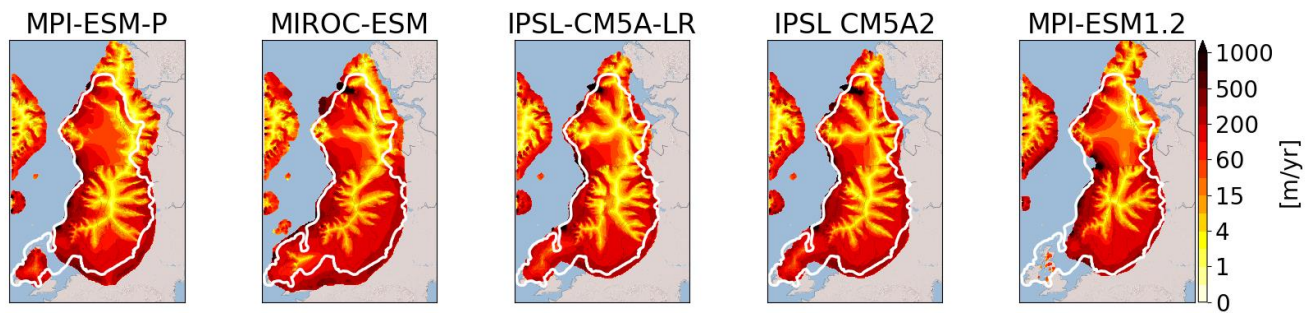
378 This allows us to use the five spin-up GRISLI experiments (forced by MPI-ESM-P, MIROC-ESM, IPSL-CM5A2,
379 IPSL-CM5-LR, and MPI-ESM1.2) as a starting point to test the sensitivity of the EIS to atmospheric, oceanic and
380 sea level forcings.



381
382 **Figure 4:** Mean summer (JJA) surface air temperature at 21 ka simulated by each GCM at the sea level and
383 interpolated on the GRISLI grid. The white line represents the ice extent as defined by the most credible DATED-
384 1 scenario.



385
386 **Figure 5:** Same as Figure 4 for the mean annual precipitation.



387

388 **Figure 6:** Simulated ice velocities at the end of the 100 000-year LGM simulation. The solid white line represents
 389 the most credible ice extent from the DATED-1 compilation.

390 4.2. Sensitivity experiments

391 In the following, we investigate the sensitivity of the Eurasian ice sheet to the potential drivers of ice sheet retreat:
 392 atmospheric changes responsible for SMB changes (i.e., temperature and snow accumulation to the first order),
 393 oceanic changes (sub-shelf melt rate) and sea level changes.

394 4.2.1 EXP1: Surface air temperature

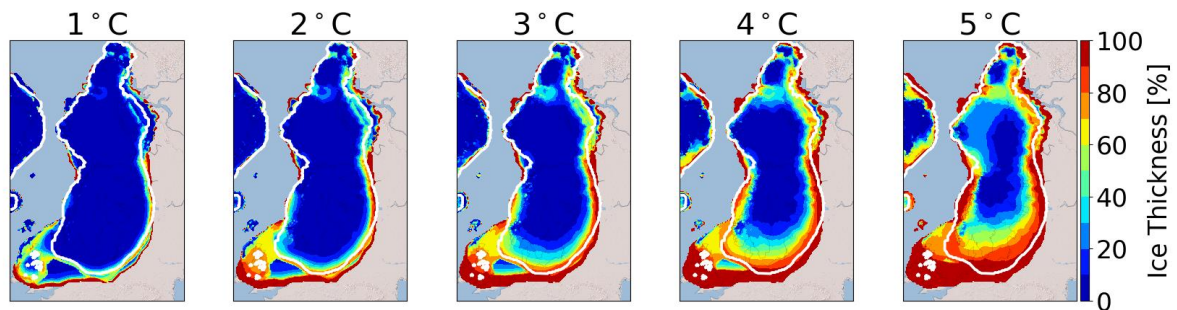
395 The aim of this section is to investigate the sensitivity of EIS to a temperature rise. For each temperature
 396 perturbation ($T_{\text{add}} = 1$ to 5°C) applied uniformly on the monthly mean surface air temperatures, Figure 7 displays
 397 for the multi-model mean the percentage of the ice thickness lost after 1000 years with respect to the initial
 398 configuration. The results are plotted for the largest ice sheet mask. This mask corresponds to all areas where ice
 399 has been simulated in at least one of the 5 simulations. This means that multi-model means are computed with 1,
 400 2, 3, 4 or 5 models involved, depending on the ice sheet mask of each individual model.

401 For $T_{\text{add}} = 1^{\circ}\text{C}$, the response of the Eurasian ice sheets is weak, except for the British Isles sector (Fig 7) for which
 402 mean JJA temperatures of the five selected GCMs are close to the melting point (Fig. 4). Substantial ice losses are
 403 also simulated in the FIS margins for temperature rise greater than 1°C leading to a progressive retreat of the edge
 404 of the ice sheet as the temperature increases. The sensitivity of the BIIS and FIS regions to these temperature
 405 perturbations is explained by a shift from positive to negative SMB values when temperature increases (Fig. SP2).
 406 By contrast, as the BKIS is located in colder areas, larger temperature perturbations (3 to 5°C) are necessary to
 407 initiate the ice sheet's retreat. The southern BKIS margin appears the most sensitive region, followed by the region
 408 of the SA ice stream. In the SA sector, ice thickness losses between 30 % ($T_{\text{add}} = +3^{\circ}\text{C}$) to 50 % ($T_{\text{add}} = +5^{\circ}\text{C}$)
 409 are obtained. In the BJR sector, ice losses are only simulated for large temperature perturbations.

410 However, it is worth mentioning that for a given temperature perturbation, significant differences in the behavior
 411 of the five simulated ice sheets can be observed. To illustrate these differences, we plotted for each simulation, the
 412 percentage of the ice thickness lost after 1000 years with respect to the initial configuration (Fig SP3). The most
 413 sensitive regions to surface air temperature, namely the FIS margins and the SA/BJR sectors, are the locations
 414 where inter-model differences in ice thickness losses are the most significant and are amplified with temperature
 415 increase. In the BJR sector, the retreat of the ice sheet is simulated for perturbations of 4°C with three GCM
 416 forcings (MIROC-ESM, IPSL-CM5A-LR and IPSL-CM5A2, Fig SP3), while this sector is stable with the two
 417 other forcings (MPI-ESM-P and MPI-ESM1.2) under this temperature perturbation. In the SA sector, the MIROC-

418 ESM-P forcing produces a retreat from a temperature anomaly of 2°C, but for the IPSL-CM5A-LR and IPSL-
419 CM5A2 forcings the retreat is only triggered for $T_{\text{add}} = 3$ °C. By contrast, the two versions of the MPI-ESM
420 produce a more stable ice sheet in the SA sector since, even with a 5 °C temperature perturbation, the ice retreat
421 is not triggered within the 1000 years of simulation.

422 The lower sensitivity of BJR sector, compared to the SA sector, can be explained (at least partly) by the topography
423 differences between these two regions. Actually, the initial topography of each GCM (not shown) exhibits a trough
424 in the SA sector which does not appear in the region of the BJR ice stream. The lower surface topography in the
425 SA sector is accompanied by higher surface temperatures and thus to larger ice losses when temperature
426 perturbations are applied (Fig. SP3). Moreover, the difference in the sensitivity of the BJR and SA sectors can be
427 also explained by the higher precipitation rate in the BJR sector (between 0.2 to 0.5 m yr⁻¹ for the BJR ice stream
428 and less than 0.2 m yr⁻¹ for the SA sector, Fig. 5), which can partly counteract the effect of temperature increase
429 on ice mass loss.



430
431 **Figure 7:** Multi-model mean of the ice thickness lost after 1000 GRISLI model years in the EXP1 experiments
432 with respect to the ice thickness of the LGM ice sheet (red: 100% lost). The results are plotted on the largest ice
433 sheet mask. The white line corresponds to the common ice sheet mask of the five models, i.e., where the multi-
434 model mean is computed on the 5 models.

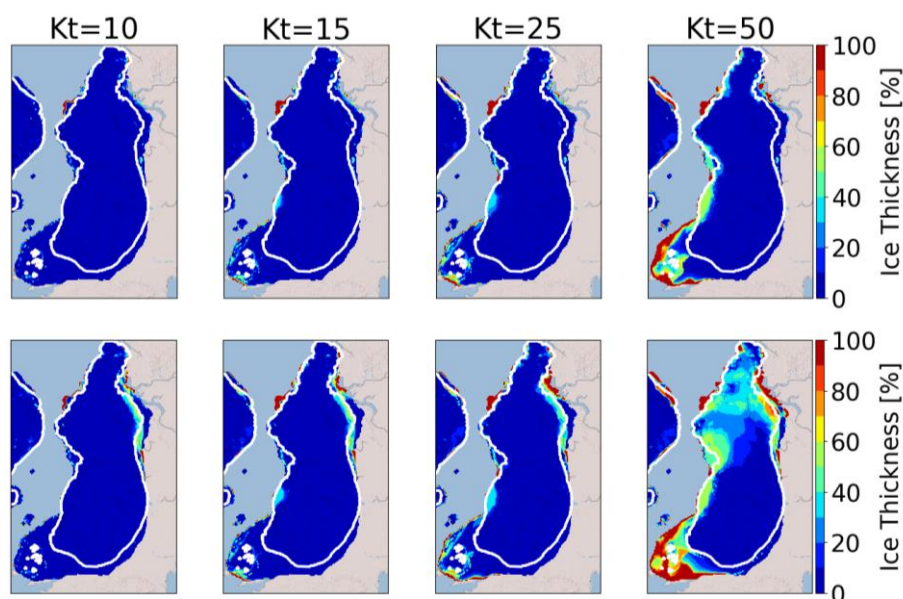
435 To better understand the effect of precipitation on the EIS stability, the EXP2 combines the precipitation and
436 surface air temperature perturbations. The results obtained in the EXP2 experiments are shown in figure SP4. For
437 BIIS and FIS, a similar behavior to EXP1 is observed, albeit with less ice melt due to increased accumulation as a
438 result of increased temperatures. On the contrary, in EXP2, a large difference with EXP1 is simulated for BKIS,
439 where only the ice sheet margins show sensitivity to increased temperature and precipitation. While an inland ice
440 loss between 20% and 50% was simulated in EXP1 in some places, it is generally limited to less than 10% in
441 EXP2. This result shows the significant role of precipitation to counteract the ice loss due to an increase in surface
442 air temperature.

443 **4.2.2 EXP3: Basal melting**

444 Besides changes in SMB, another factor that can destabilize a marine ice sheet is the basal melting under the ice
445 shelves (Pritchard et al., 2012). In the LGM experiments, the numerical Kt value is fixed to 7 m °C⁻¹ yr⁻¹ and leads
446 to basal melting rates in the BJR and SA sectors of 3.1 m yr⁻¹ and 0.7 m yr⁻¹ respectively. To investigate the effect
447 of increased basal melting that likely occurred during the last deglaciation as a response of increased ocean
448 temperatures, we performed sensitivity experiments by first changing the Kt value (EXP3.1). The sensitivity to
449 oceanic temperatures (EXP3.2) will be discussed later.

450 Figure 8 displays the percentage of ice thickness losses (with respect to the initial configuration) for Kt ranging
451 from $10 \text{ m } ^\circ\text{C}^{-1} \text{ yr}^{-1}$ to $50 \text{ m } ^\circ\text{C}^{-1} \text{ yr}^{-1}$. After 1000 years of simulation, no change in ice thickness is observed for Kt
452 $= 10 \text{ m } ^\circ\text{C}^{-1} \text{ yr}^{-1}$. For higher Kt values ($15 \text{ m } ^\circ\text{C}^{-1} \text{ yr}^{-1}$ and $25 \text{ m } ^\circ\text{C}^{-1} \text{ yr}^{-1}$), ice losses between 30% to 40% are
453 simulated in the MN ice stream sector, and 100% of the ice shelf in the south of SA sector is melted (see Fig 3
454 showing the presence of ice shelves at the end of the spin-up experiment). This corresponds to basal melting rates
455 (multi-model mean) near the grounding line ranging from 7.5 m yr^{-1} ($Kt = 15 \text{ m } ^\circ\text{C}^{-1} \text{ yr}^{-1}$) to 10.4 m yr^{-1} ($Kt = 25$
456 $\text{ m } ^\circ\text{C}^{-1} \text{ yr}^{-1}$) in the MN sector and from 1.7 m yr^{-1} ($Kt = 15 \text{ m } ^\circ\text{C}^{-1} \text{ yr}^{-1}$) to 2.9 m yr^{-1} ($Kt = 25 \text{ m } ^\circ\text{C}^{-1} \text{ yr}^{-1}$) in the SA
457 sector. However, these changes are restricted to small areas, and the ice loss is not significant enough to firmly
458 indicate a noticeable sensitivity to basal melting. Perturbations with Kt values above $25 \text{ m } ^\circ\text{C}^{-1} \text{ yr}^{-1}$ are necessary
459 to observe significant changes in the EIS configuration. In particular, for $Kt = 50 \text{ m } ^\circ\text{C}^{-1} \text{ yr}^{-1}$, the ice is entirely
460 melted near the BIIS margins, and less than 50 % of the ice remains in the regions of MN, SA and BJR ice streams.
461 Nonetheless, only the simulations forced by MPI-ESM-P, MPI-ESM1.2 and MIROC-ESM show a sensitivity to
462 basal melting in BJR, MN and SA sectors (Fig. SP5). Depending on the GCM forcing, the simulated basal melting
463 values range between 25.7 and 28.7 m yr^{-1} , 24.4 and 28.2 m yr^{-1} and between 11.2 and 13.4 m yr^{-1} for the BJR,
464 MN and SA sectors respectively. By contrast, very small values are obtained with IPSL-CM5A2 (0.2 m yr^{-1} – 0.5 m
465 yr^{-1}) and IPSL-CM5A-LR models (0.5 m yr^{-1}). This can be explained by the cold oceanic temperatures near the
466 BJR sector compared to those simulated by the three other GCMs (Fig SP6). These results show that the basal
467 melting has the ability to destabilize the BKIS when it exceeds a certain threshold. Results inferred from the
468 simulations forced by MPI-ESM-P, MPI-ESM1.2 and MIROC-ESM suggest that this threshold is obtained for Kt
469 values between 25 and $50 \text{ m } ^\circ\text{C}^{-1} \text{ yr}^{-1}$, corresponding to basal melting rates at the grounding line between 10.4 m
470 yr^{-1} and 28.7 m yr^{-1} for the BJR sector and between 6.2 and 13.4 m yr^{-1} for the SA sector. By comparison, a basal
471 melting rate of 22 m yr^{-1} has been observed thanks to radar measurements in the mouth of the Mercer/Whillans Ice
472 Stream located in the West Antarctic ice sheet (Marsh et al., 2016). Providing that Kt values are greater than 25 m
473 $\text{ } ^\circ\text{C}^{-1} \text{ yr}^{-1}$ (or close to $50 \text{ m } ^\circ\text{C}^{-1} \text{ yr}^{-1}$), the region of the BJR ice stream responds to basal melting perturbations with
474 basal melting rates similar to those observed in some parts of WAIS. However, the ice loss is restricted to the very
475 edge of the ice sheet and the BKIS retreat is negligible. This raises the question as to whether the basal melting
476 exerts a stronger influence on longer time scales. Therefore, we also investigated the ice sheet behavior after 10 000
477 model years.

478



479

480 **Figure 8:** Multi-model mean of the ice thickness lost after 1000 (top) and 10 000 (bottom) GRISLI model years
 481 in the EXP3.1 experiments with respect to the ice thickness of the LGM ice sheet. (red: 100% lost). The white line
 482 corresponds to the common ice sheet mask of the five models, i.e., where the multi-model mean is computed on
 483 the 5 models.

484 A similar behavior is observed after 10 000 years for Kt between 10 and 25 $\text{m } ^\circ\text{C}^{-1} \text{ yr}^{-1}$, with the exception of the
 485 southern part of BKIS bordering the Kara Sea where a 30% to 50% ice thickness decrease, with respect to the
 486 initial one, is obtained. For Kt=50 $\text{m } ^\circ\text{C}^{-1} \text{ yr}^{-1}$, more than 40% of ice loss is simulated for BKIS, and up to 60% in
 487 the BJR sector. As previously mentioned, this large ice thickness decrease in the center of BKIS is highly GCM-
 488 dependent, and is only observed in simulations forced by the MIROC and MPI models (Fig. SP5)

489 As the basal melting parameterization is expressed as a quadratic function of the oceanic temperatures, we may
 490 expect a different sensitivity of EIS when the oceanic temperatures increase (EXP3.2). Results of the EXP3.2
 491 experiments are shown in figure SP7. Perturbations of oceanic temperatures between $+0.5^\circ\text{C}$ and $+1.5^\circ\text{C}$ lead to
 492 basal melting rates at the grounding line of the BJR sector of less than 3.8 m yr^{-1} . This is well below the threshold
 493 suggested by the results of the EXP3.1 experiments (between 10.4 and 30 m yr^{-1}), and no significant ice loss is
 494 simulated after 10 000 years of simulation.

495 For larger perturbations ($+7.5^\circ\text{C}$ and $+10^\circ\text{C}$), larger values of the basal melting rates are obtained in the BJR (11.6
 496 and 17.5 m yr^{-1}), in the SA (10.8 and 15.6 m yr^{-1}) and in the MN sectors (11.5 and 17.4 m yr^{-1}) after 10 000 model
 497 years. A perturbation of 7.5°C does not trigger the ice retreat because of a too low basal melting. By contrast, when
 498 the perturbation reaches $+10^\circ\text{C}$, a similar behavior to that simulated with Kt=50 $\text{m } ^\circ\text{C}^{-1} \text{ yr}^{-1}$ (EXP3.1) is obtained.

499 On the other hand, for simulations forced by IPSL-CM5A2 and IPSL-CM5A-LR, an increase in oceanic
 500 temperatures of $+10^\circ\text{C}$ allows us to observe a sensitivity of BKIS in the SA sector (see Fig SP8) after 1000 years
 501 of simulations, which leads to a total retreat of the eastern part of BKIS after 10000 years.

502 These results show that the BJR, MN and SA regions are sensitive to sub-shelf melting providing that the basal
 503 melt exceeds a certain threshold obtained for Kt values greater than $25 \text{ m } ^\circ\text{C}^{-1} \text{ yr}^{-1}$ (and greater than $10 \text{ m } ^\circ\text{C}^{-1} \text{ yr}^{-1}$

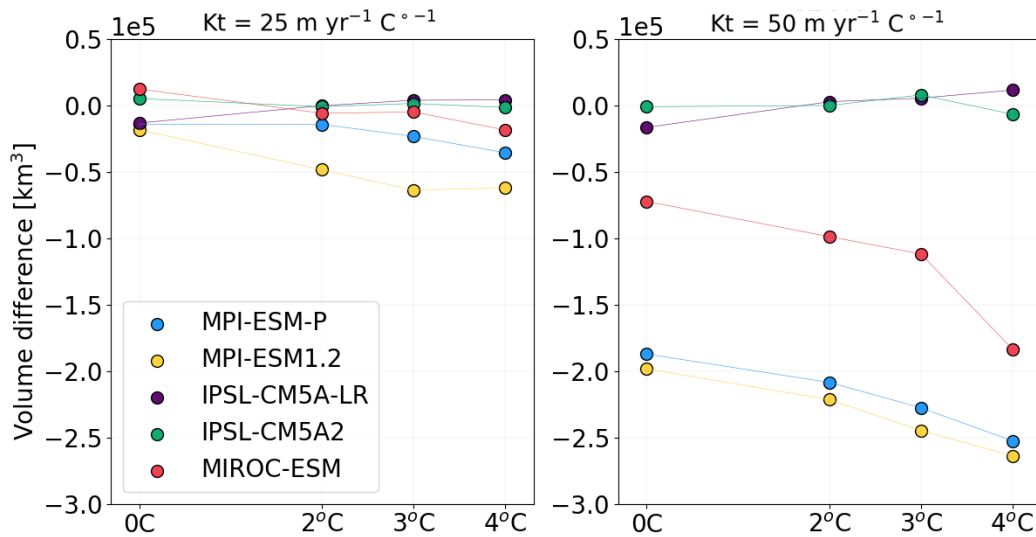
504 for the MN sector) or for a rise in oceanic temperature greater than 7.5°C. From the combination of EXP3.1 and
505 EXP3.2 experiments, it appears that the threshold is between 11.6 m yr⁻¹ and 17.5 m yr⁻¹ for the BJR sector,
506 between 6.2 and 13.4 m yr⁻¹ for the SA sector and lower than 7.5 m yr⁻¹ for the MN sector. Moreover, our results
507 also suggest that the large retreat of one single ice stream has the ability to favor the total retreat of the whole of
508 BKIS

509 **4.2.3 EXP4: Combined effects of basal melting and surface air temperatures**

510 Results presented in the previous section suggest that sub-shelf melting has only a poor impact on the EIS
511 destabilization for Kt perturbations below a certain threshold estimated to lie between 25 and 50 m °C⁻¹ yr⁻¹, or
512 below a +10°C increase of oceanic temperatures. However, increases in surface melting due to atmospheric
513 warming may lead to changes in the geometry of the grounded ice sheet and floating ice shelves. In turn, changes
514 in the EIS configuration may alter the EIS sensitivity to basal melting. To test this hypothesis, we combined surface
515 air temperature perturbations with basal melting perturbations (EXP4) and compared the results with those of the
516 EXP1 experiments. Figure 9 displays the difference in the total BKIS ice volume after 1000 years between EXP4
517 and EXP1 experiments (ΔV_{4-1}) for different surface atmospheric temperature perturbations ($\Delta T = +2^\circ\text{C}$, $+3^\circ\text{C}$
518 and $+4^\circ\text{C}$) and Kt values fixed to 25 and 50 m °C⁻¹ yr⁻¹ (negatives values are associated to a greater ice loss in
519 EXP4 than in EXP1). For both Kt perturbations (Kt = 25 and 50 m °C⁻¹ yr⁻¹), no significant difference in the ΔV_{4-1}
520 values (computed for the different ΔT perturbations) is observed in simulations forced by IPSL-CM5A2 and IPSL-
521 CM5A-LR. This illustrates the poor sensitivity of BKIS to basal melting with the IPSL climate forcings. As
522 explained in section 4.2.2, this low sensitivity is due to the cold oceanic temperatures simulated in both IPSL
523 models (see Fig. SP6). For the three other simulations (forced by MIROC-ESM, MPI-ESM-P, and MPI-ESM1.2),
524 the ice volume difference is clearly amplified with higher ΔT levels, especially when the Kt transfer coefficient is
525 higher. For example, for Kt=50 m°C⁻¹yr⁻¹, the difference in ΔV_{4-1} values between the initial ice sheet configuration
526 ($\Delta T = 0^\circ\text{C}$) and $\Delta T = 4^\circ\text{C}$ is ~60 000 km³ with MPI-ESM-P, against ~20 000 km³ when Kt=50 m°C⁻¹yr⁻¹. A
527 similar behavior is observed for simulations forced by MIROC-ESM (~110 000 km³) and MPI-ESM1.2 (~60 000
528 km³). To better illustrate the impact of the combination of both temperature and basal melting perturbations, we
529 plotted the evolution of ice loss every 1kyr as simulated in the EXP1 ($\Delta T = +4^\circ\text{C}$), EXP3 (Kt=50 m°C⁻¹yr⁻¹) and
530 EXP4 experiments in figures SP9 to SP11. For the simulation forced by MIROC-ESM (Fig. SP11), the largest part
531 of the deglaciation signal is dominated by increased atmospheric temperatures in the EXP4 (see Fig SP11).
532 Simulations forced by MPI-ESM-P and MPI-ESM1.2 have a different behaviour (Figs SP9 and SP10) and show a
533 significant difference between EXP1 and EXP4 and between EXP3 and EXP4. In the EXP3 experiment, the SA
534 sector appears to be highly sensitive, mainly due to high ocean temperatures (> 3°C, see fig SP6) in contrast to the
535 BJR sector where only a part has deglaciated after 10 000 years. However, in the EXP4 experiment, in which near-
536 surface temperature and basal melting are combined, BKIS starts to retreat after 1000 years and has almost entirely
537 melted after 10 000 years. This suggests that the BKIS deglaciation is initially triggered by surface warming but
538 is further amplified by basal melting.

539

540



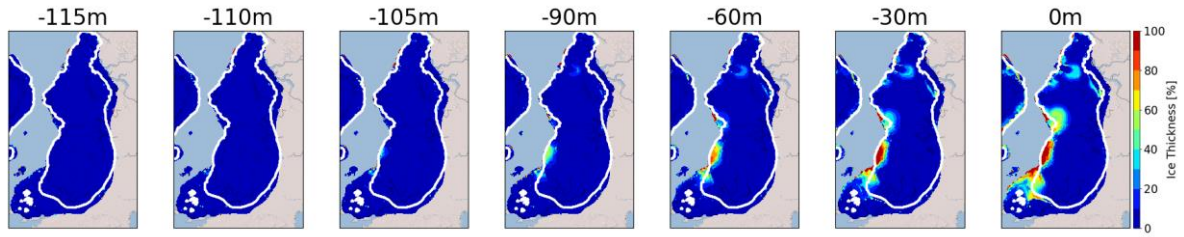
541
 542 **Figure 9:** Differences of the ice volume lost between EXP4 and EXP1 ($\Delta V_{+1}(\Delta V_{+1})$) after 1000 years for $Kt=25$
 543 $m\ ^\circ C^{-1}\ yr^{-1}$ (left) and $Kt=50\ m\ ^\circ C^{-1}\ yr^{-1}$ (right).

544 **4.2.5 Exp5: Sea level**

545 In the previous simulations, the sea level forcing was fixed to -120 m (with respect to the present-day eustatic sea
 546 level), corresponding to the estimated eustatic level at the LGM (Peltier et al., 2002). In this series of experiments,
 547 we quantify the sensitivity of the EIS to different sea level forcings.

548 The multi-model mean difference between the ice thickness after 1000 GRISLI model years and the initial ice
 549 thickness (sea level = -120 m) is displayed in Figure 10 for the different sea level elevations ranging from -115_m
 550 to 0 m. After 1000 years of simulation, for sea levels ranging from -115 m to -105 m, no significant differences
 551 are observed with respect to the reference simulation (i.e., -120 m). For larger perturbations, the MNIS sector
 552 appears to be the most sensitive. As an example, for a sea level of -90 m, an ice loss of ~40 % is simulated in this
 553 area, and an almost complete retreat is obtained for a sea level higher than -60m, with an ice thickness decrease of
 554 up to 80%-100%. Although sea level elevations of -90 m and -60 m are considerably larger than the global mean
 555 sea level at the LGM, they are consistent with the local sea level variations that could be as high as -70 m as
 556 suggested by Gowan et al. (2021). However, for the other sectors (BJR, SA, NCIS), ice thickness decrease is only
 557 obtained for sea levels higher than -30 m which is largely out of the range advanced by Gowan et al. (2021). As a
 558 result, this series of experiments ~~suggest~~suggests ~~conducted with the GRISLI model suggests~~ that the elevation of sea level
 559 has only played a marginal role at the beginning of the EIS deglaciation.

560 However, it should be noted that sea level rise can lead to changes in the geometry of the ice sheet and floating ice
 561 shelves. Therefore, these changes in the EIS configuration may influence its sensitivity to oceanic temperature
 562 perturbations. We tested this hypothesis by raising the sea level from -120 m to -110 m compared to the current
 563 level and by raising concomitantly the oceanic temperatures (+1.5°C and +10°C). Adding a sea level perturbation
 564 to the oceanic temperature perturbation does not drastically change the response of the ice sheet. Differences of 6
 565 to 7 % in ice volume losses were only observed for the highest temperature perturbation (+10°C) after 10 000
 566 years for only two GCM forcings (MIROC-ESM and IPSL-CM5A2), while the differences are negligible (lower
 567 than 2%) for smaller perturbations, shorter timescales and other GCM forcings (not shown).



568

569 **Figure 10:** Multi-model mean of the ice thickness lost after 1000 model years in the EXP5 with respect to the ice
 570 thickness of the LGM ice sheet. (red: 100% lost). The white line corresponds to the common ice sheet mask of the
 571 five models, i.e., where the multi-model mean is computed on the 5 models.

572 4.3 Sensitivity to the spin up method

573 The construction of spin-up is one of the most important factors impacting the sensitivity of the EIS. The LGM
 574 ice sheets presented in Section 4.1 were constructed under a constant LGM climate during 100 000 years. The
 575 specificity of this method is to construct ice sheets in good equilibrium with their environment. However, as
 576 outlined by Batchelor et al. (2019), the EIS was far from being in equilibrium with the climate at the LGM.

577 In order to look into the biases associated with the choice of the spin-up method, we compared the results obtained
 578 with a transient spin-up procedure. For this purpose, we reconstructed a climatology evolving from the Last
 579 Interglacial (-127 000 years) to the LGM (-21 000 years) using a multi-proxy climatic index (Quiquet et al., 2021c).
 580 In the same way as above, we used the 10 PMIP3/PMIP4 forcings shown in Table 1. As the last interglacial
 581 simulations were not available for some of the PMIP3/PMIP4 models, we made the approximation that the -127
 582 000 climate was represented by the pre-industrial climate (i.e. piControl experiments, Eyring et al., 2016).

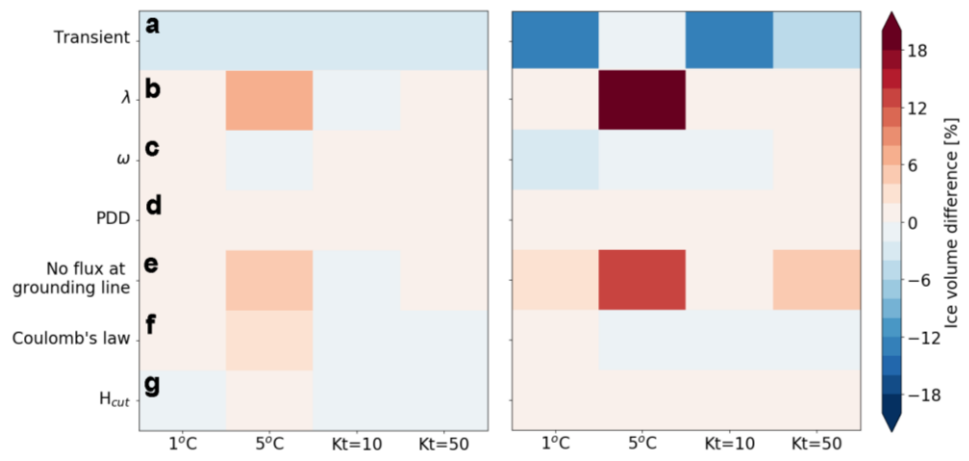
583 At the end of the of these new spin-up simulations, only 4 PMIP forcings (MPI-ESM-P, MPI-ESM1.2, IPSL-
 584 CM5A2 and IPSL-CM5A-LR) succeeding in constructing the EIS in agreement with the reconstructions (see
 585 figure SP12h). Compared to previous LGM ice sheets presented in Section 4.1, the ice extent is smaller (Fig.
 586 SP12h) and the dome of FIS is flatter with sharper edges. Furthermore, contrary to the previous method of spin-
 587 up construction (i.e. constant LGM forcing), the simulation forced by MIROC-ESM failed to form an ice sheet
 588 over the Barents Sea.

589 To assess the effect of the LGM EIS obtained after each of the transient spin-up experiment obtained with MPI-
 590 ESM-P, MPI-ESM1.2, IPSL-CM5A2 and IPSL-CM5A-LR, we applied atmospheric temperature perturbations
 591 (+1°C and +5°C, as in EXP1) and basal melting perturbations (Kt values of 10 m°C⁻¹yr⁻¹ and 50 m°C⁻¹yr⁻¹, as in
 592 EXP3.1). Finally, we compare the percentage of remaining ice volume with the reference one (i.e simulated in
 593 EXP1 and EXP3.1) and the new perturbed simulations after 1000 and 10 000 years using the following formula:

594
$$\delta = \frac{V_{pert}(t=end) - V_{pert}(t=0)}{V_{pert}(t=0)} - \frac{V_{ref}(t=end) - V_{ref}(t=0)}{V_{ref}(t=0)} \quad (8)$$

595 Each term in the right-hand side of Equation (8) represents the percentage of ice volume loss in a given simulation.
 596 δ represents the difference (in %) of ice volume loss between the new simulation and the reference simulation,
 597 with V_{pert} being the ice volume for the new perturbed simulation (transient spin-up) and V_{ref} the ice volume of
 598 the EXP1 and EXP3 simulations. A negative value of V_{ice} indicates a greater retreat of EIS of the new EIS
 599 configurations (i.e. obtained with the transient spin-up method).

600 Figure 11a shows the results of the computed δ value (see Eq. 8) after 1000 (left) and 10 000 model years (right)
 601 averaged over all models for atmospheric (1°C and 5°C) and oceanic (Kt = 10 and 50 m°C⁻¹yr⁻¹) perturbations.
 602 After 1000 years, no significant difference is observed between both simulations. Conversely, after 10 000 years,
 603 a difference of the order of -10% for perturbations of 1°C and 10 m°C⁻¹yr⁻¹ is observed. This can be explained by
 604 internal processes that are not in equilibrium with the LGM climate at the end of the transient spin-up simulation.
 605 More specifically, large differences in the simulated effective pressure are obtained at the end of both spin-up
 606 experiments. In the reference spin-up simulation (constant LGM climate), there is a relatively low effective
 607 pressure since sub-glacial water has accumulated over the 100 000 year of simulation (Fig. SP13). By contrast, in
 608 the spin-up constructed by the transient method, large parts of the ice sheet are englacial for much shorter time
 609 periods with smaller amount of sub-glacial water resulting in higher effective pressure. This leads to drastically
 610 different sliding velocities among the two spin-up methods, with much smaller ice sheet velocities after the
 611 transient spin-up. During the perturbation experiments, the sub-glacial water tends to accumulate when using the
 612 transient spin-up ice sheet state. The temporal evolution in this case reflects the decrease in the effective pressure
 613 (and related increase in velocity) on top of the applied atmospheric or oceanic perturbation. The sensitivity over
 614 time scales greater than one thousand years in these new experiments is thus not directly comparable to the
 615 reference sensitivity experiments in which the effective pressure is fully equilibrated.



616 Figure 11: Multi model mean of the differences in ice volume loss between the new perturbed simulations and the
 617 reference simulations (EXP1 and EXP3) after 1000 years (left) and after 10000 years (right). Note that the multi
 618 model mean is done without the contribution of MIROC-ESM forcing for the panel a. The volume difference is
 619 calculated thanks to the equation 8.
 620

621 4.4 Sensitivity to different GRISLI configurations

622 The results presented in Section 4.2 suggest that the EIS was primarily sensitive to atmospheric forcing at the
 623 beginning of the last deglaciation. However, we cannot exclude that this finding is specific to the choices of model
 624 parameters (Table 2) and physical parameterizations (Table 3). In order to assess the extent to which the observed
 625 EIS sensitivity is driven by these choices, we conducted additional experiments with alternative values of climate-
 626 related parameters (vertical temperature gradient, the precipitation ratio to temperature change, degree-day factors
 627 in the PDD formulation). We also changed the basal friction law and removed the parameterization of the ice flux
 628 at the grounding line (Table 4). We first performed 100 000-year simulations using the same procedure as for the

629 reference simulations (Fig. SP12a-g). Note that the CNRM-CM5, GISS-E2-R, MIROC-ES2L, FGOALS-G2 and
 630 MRI-CGM3 fail to reproduce an ice sheet in agreement with the reconstructions similarly to as our reference
 631 experiments (see Sections 4.1 and 4.2).

632 Next, we applied atmospheric temperature perturbations (+1°C and +5°C) and basal melting perturbations ($K_t =$
 633 10 m°C⁻¹yr⁻¹ and 50 m°C⁻¹yr⁻¹) to evaluate the relative importance of both atmospheric and oceanic forcings with
 634 the modified GRISLI configurations.

635 **Table 4:** List of sensitivity experiments (columns 5-10) performed with changes in the standard GRISLI
 636 configuration. New values of model parameters are given in column 4 with reference values indicated in
 637 parentheses. Changes in physical parametrizations are indicated in column 2.

exp	GRISLI configuration changes			Spin-up methods		Perturbations experiments			
	Variables	Name	Value	Constant LGM	Transient	1°C	5°C	Kt=10	Kt=50
<u>1</u>	<u>Spin-up method</u>	-	<u>Transient</u>		✓	✓	✓	✓	✓
<u>2</u>	<u>Vertical temp gradient</u>	λ	<u>4 °C km⁻¹ (7)</u>	✓		✓	✓	✓	✓
<u>3</u>	<u>Precip/temperature change</u>	ω	<u>0.05 °C⁻¹ (0.11)</u>	✓		✓	✓	✓	✓
<u>4</u>	<u>PDD coefficients</u>	$C_{ice,snow}$	<u>- 25%</u>	✓			✓	✓	✓
<u>5</u>	<u>PDD coefficients</u>	$C_{ice,snow}$	<u>+ 25%</u>	✓		✓			
<u>6</u>	<u>Flux at the grounding line</u>	-	<u>None</u>	✓		✓	✓	✓	✓
<u>7</u>	<u>Basal friction law</u>	-	<u>Plastic drag</u>	✓		✓	✓	✓	✓
<u>8</u>	<u>calving criterion</u>	H_{cut}	<u>50 m (250)</u>	✓		✓	✓	✓	✓

638

639 **4.4.1 Sensitivity to climate parameters**

640 At first, we examined the sensitivity of EIS to a vertical temperature gradient of 4 °C km⁻¹ (instead of 7 °C km⁻¹)
 641 which is considered by Marshall et al. (2007) as the most likely value of the near-surface temperature lapse rate.
 642 Therefore, a decrease in ice thickness of 100 meters results in a decrease in atmospheric temperature of 0.4 °C
 643 instead of 0.7 °C (see Eq. 4). This choice aims at reducing the sensitivity of EIS to atmospheric forcing in order to
 644 analyze whether the ice sheet is more responsive to the oceanic forcing.

645 Secondly, in EXP2, we found that increased precipitation as a result of increased temperatures (see Eq. 5) tends to
 646 reduce the sensitivity of EIS. In the reference simulations (Section 4.2), the precipitation ratio to temperature
 647 change (ω value) was set to 0.11°C⁻¹. However, lower values can be found in the literature ranging between 0.05
 648 °C⁻¹ and 0.11 °C⁻¹ (Petrini et al., 2020, Charbit et al., 2013, Quiquet et al., 2013). We therefore investigated
 649 whether the choice of a lower precipitation-temperature ratio, which is expected to lower the precipitation
 650 dependency to temperatures, could influence the response of the EIS. In this new series of sensitivity experiments,

651 the ω parameter was fixed to $0.05 \text{ }^\circ\text{C}^{-1}$. In doing so, our objective is to assess whether a variation in ω can lead to
652 significant changes in the response of the ice sheet to atmospheric forcing.

653 At last, Charbit et al. (2013) demonstrated that that the choice of the PDD formulation can have a substantial
654 impact on the computed amount of ice melt. In order to assess the impact on the stability of the EIS of the melt
655 coefficient C_{ice} and C_{snow} , as defined in Tarasov and Peltier (2002), we decreased (resp. increased) their values
656 by 25% for the $+5^\circ\text{C}$ (resp. $+1^\circ\text{C}$) temperature perturbation. Decreasing (resp. increasing) the melt coefficients by
657 25% for the temperature perturbations allows to reduce (resp. increase) the influence of the atmospheric forcing
658 on the evolution of the EIS. In addition, in order to reduce the influence of the surface air temperatures, we have
659 also tested the impact of decreased melt coefficients in the basal melting perturbation experiments.

660 The results of these new sensitivity experiments are analyzed in terms of differences in ice volume loss at years
661 1000 and 10 000 years with the reference simulations (δ value, see Eq. 8) and are displayed in figure 11 (b-d). The
662 only significant differences with the reference simulations are obtained for a 5°C perturbation due to a lowered
663 temperature-elevation feedback in the simulation with $\lambda = 0.4 \text{ }^\circ\text{C km}^{-1}$. For all the other experiments changes in
664 the ω parameter or in the degree-day factors, differences with reference simulations are less than + 2%. As
665 such, this series of perturbed experiments shows that changing climate-related model parameters results in only
666 small changes in the EIS ice volume loss compared to the standard configuration of the GRISLI ice-sheet model,
667 and does not question the prevailing influence of the atmospheric forcing suggested by our reference sensitivity
668 experiments.

669 **4.4.2 Sensitivity to physical parameterizations**

670 Besides the climate related parameters, changes in the representation of the dynamic processes may have a strong
671 impact on the relative importance of the mechanisms responsible for the triggering of the EIS retreat. For example,
672 using the PSU ice sheet model (Pollard and De Conto, 2012), Petrini et al. (2018) found that the implementation
673 of a grounding line flux adjustment reduces the sensitivity of BKIS. To go a step further and compare our findings
674 with those of Petrini et al. (2018), we removed the grounding line flux parameterization in the GRISLI model and
675 assessed its impact on the EIS sensitivity. Without the flux adjustment, the EIS sensitivity to basal melting and
676 atmospheric temperature perturbations is reduced (Fig. 11e). This contrasts with the findings of Petrini et al (2018).
677 More specifically, after 10 000 years, a $+5^\circ\text{C}$ atmospheric perturbation results in a reduced amount of melting of
678 about 14% compared to the reference experiment (with parameterization of the grounding line flux). In other
679 words, these results suggest that in the absence of the grounding line flux adjustment, higher atmospheric
680 temperatures can potentially enhance the ice sheet's sensitivity to oceanic forcing through grounding line retreat.

681 Another source of huge uncertainties lies in the choice of the basal friction law (e.g. Brondex et al., 2017, Joughin
682 et al., 2019; Akesson et al., 2021). An appropriate choice of this law is of primary importance as basal friction
683 exerts a strong control on the dynamics of the grounding line and fast-flowing ice streams. In our previous
684 experiments, the basal friction was parameterized using a linear dragging law (Eq. 2). In order to investigate the
685 extent to which the choice of the friction law can influence the sensitivity of the EIS to atmospheric temperature
686 and basal melting perturbations we used a plastic dragging law where the basal drag depends quadratically on the
687 basal velocity (Pattyn et al., 2017).

688 In contrast to previous works investigating the ice sheet sensitivity to friction laws, our findings reveal that
689 experiments using the non-linear basal friction do not exhibit significant differences compared to EXP1 and EXP3
690 simulations after 1,000 and 10,000 years (Fig. 11f). However, it is important to note that Joughin et al. (2019) and
691 Akesson et al. (2021) explored the sensitivity of the Antarctic ice sheet, which differs from the EIS configuration.
692 This may explain (at least partly) why the EIS may exhibits a different sensitivity to changes in the friction law.

693 Thinning of confined ice shelves through basal melting produce a weakening of the buttressing effect, implying
694 an acceleration of the grounded ice streams and ultimately a substantial ice discharge in the ocean. This sequence
695 of events was observed in the Antarctic Peninsula after the collapse of the Larsen B Ice Shelf in 2002 (Rignot et
696 al., 2004; De Rydt et al., 2015). In our reference experiments, the ice shelf extent is small (Fig. 3). This likely
697 explains why the EIS appears poorly sensitive to basal melting. In order to potentially increase the area of ice
698 shelves, we reduced the calving criterion from 250 m to 50 m. This results in a slight increase of the ice shelf area
699 at the LGM (Fig. SP12d) compared to the reference simulations (Fig 3). However, this increase did not result in a
700 substantial change of the sensitivity of the EIS to basal melt and atmospheric temperature perturbations (Fig. 11g).
701 This limitation is due to the topography, which does not allow for adequate confined ice shelf development, unlike
702 the Antarctic, where the presence of bays (in Ross and Weddell Seas for example) allows the formation of confined
703 ice shelves.

704 Thus; as previously highlighted for the GRISLI climate-related parameters, changing the parameterizations related
705 to ice dynamics does not modify the main conclusion related to the dominating effect of the atmospheric forcing
706 compared to the oceanic forcing.

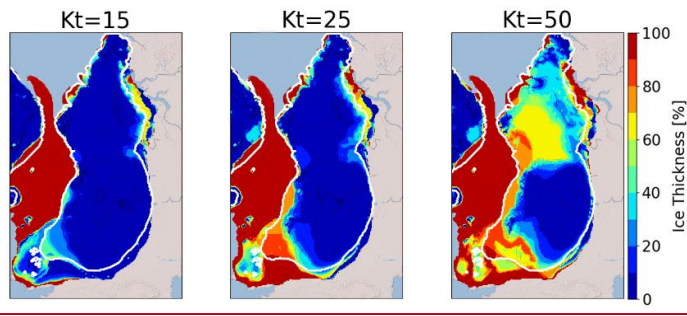
707 **5. Discussion**

708 The results of our experiments suggest that the EIS ice sheet is very sensitive to the atmospheric warming that may
709 have occurred at the beginning of the last deglaciation. By contrast, basal melting does not seem to be a key process
710 for triggering the ~~retreat of the~~ ice sheet retreat. However, once the ~~retreat has been initiated by the~~ atmospheric
711 warming has initiated the retreat, basal melting has the capability of accelerating the retreat, as supported by the
712 results of EXP4, providing that the amount of basal melting is high enough. Nevertheless, these conclusions are
713 strongly dependent on the ice-shelf configurations. Indeed, unconfined ice shelves do not exert an efficient
714 buttressing effect (i.e., the stress that the ice shelves exert at the grounding line) and their removal has almost no
715 impact on the dynamics of the grounded ice sheet (Gundmundsson et al., 2013, Fürst et al., 2016). ~~By contrast,~~
716 ~~thinning of confined ice shelves through basal melting produce a weakening of the buttressing effect, implying an~~
717 ~~acceleration of the grounded ice streams and ultimately a substantial ice discharge in the ocean. This sequence of~~
718 ~~events was observed in the Antarctic Peninsula after the collapse of the Larsen B Ice Shelf in 2002 (Rignot et al.,~~
719 ~~2004; De Rydt et al., 2015).~~ ~~Moreover, using a high resolution ice sheet model (500 mx500 m near the grounding~~
720 ~~line), Gandy et al. (2018) showed the significant impact of the melting of confined ice shelves on the destabilization~~
721 ~~of ice streams in Northwest Scotland during the last deglaciation. In our study, the extent of the confined ice~~
722 ~~shelves in the simulated EIS at the end of the spin-up experiments is very small (Fig. 3). This likely explains why~~
723 ~~the EIS appears poorly sensitive to basal melting and why strong perturbations of the Kt coefficient or oceanic~~
724 ~~temperatures are required to simulate ice shelf thinning in the regions of the main ice streams.~~

725 The small sensitivity to the oceanic forcing simulated in the EXP3 experiments contradicts the conclusions of
726 previous modeling studies of the EIS behavior during the last glacial period (Alvarez-Solas et al., 2019) and the
727 last deglaciation (Petrini et al., 2020). Both conclude that oceanic temperatures are the main driver of the EIS
728 destabilization. Their findings are all the more surprising as they both use an ice-sheet model (GRISLI1.0) similar
729 to ours (GRISLI2.0). However, several differences can be noticed between their modeling approach and that of
730 the present study. First, GRISLI1.0 does not include a parameterization of the ice flux at the grounding line.
731 Therefore, it should be easier with our model to trigger the EIS retreat through basal melting because GRISLI2.0
732 includes key processes to simulate the marine ice sheet instability. To verify this issue, we performed additional
733 simulations similar to the EXP3 ones by removing the grounding line flux parameterization, and as expected,
734 results clearly show that the removal of this parameterization limits the ice loss (not shown). One of the most likely
735 explanation of the disagreement between our findings and those of previous studies (Alvarez-Solas et al., 2019;
736 Petrini et al., 2020) relies on the procedure followed in the spin-up experiments. Both built their initial state in the
737 same way. To favor the EIS build-up, they fixed the basal melting to 0.1 m yr^{-1} during their ice sheet spin-up.
738 Starting from the EIS configuration obtained at the end of the ~~spin~~ spin-up experiment, they used a linear (Alvarez-
739 Solas et al., 2019) or quadratic (Petrini et al., 2020) basal melting parameterization depending on the oceanic
740 temperature to simulate the last glacial period (Alvarez-Solas et al., 2019) or the last deglaciation (Petrini et al.,
741 2020) of EIS. In doing so, there is a methodological inconsistency between the spin-up simulation and the
742 subsequent experiments. To investigate the effect of such inconsistency on the EIS deglaciation, we followed their
743 spin-up methodology (homogeneous basal melting) instead of the one described in Section 2.3. The resulting LGM
744 ice sheets resemble those presented in Sec. 3.1, except that the MIROC-ESM forcing produces large ice shelves
745 in the Greenland and Norwegian seas. We then applied the same perturbations as in EXP3 on these alternative ice
746 sheets with a basal melting parameterization depending on the oceanic temperature and salinity (see Eq7). We
747 display in ~~figure 11~~ Figure 12 the percentage of ice thickness lost after 10000 years with respect to the initial
748 configuration for K_t ranging from 15 to $50 \text{ m }^\circ\text{C}^{-1} \text{ yr}^{-1}$ for this new series of experiments. Compared to EXP3, we
749 show that the EIS now presents a much more significant sensitivity in the BIIS and FIS for a perturbation of $K_t=50$
750 $\text{ m }^\circ\text{C}^{-1} \text{ yr}^{-1}$. These results illustrate the extent to which the conclusions drawn for the driving mechanisms of the
751 EIS destabilization ~~are strongly dependent~~ depend on the initial state. However, we argue that the approach
752 followed in the present paper is more consistent as the basal melting parameterization is exactly the same for the
753 spin-up procedure and the sensitivity experiments.

754 ~~Finally, another~~ Another difference that deserves to be mentioned is that Petrini et al, (2020) used a ~~climate~~ climatic
755 index (based on the transient simulation of Liu et al., (2009). This method ensures that both the atmospheric and
756 oceanic temperatures increase concomitantly up to their pre-industrial levels. As a result, we cannot exclude that
757 the key role of basal melting in their simulated deglaciation is not amplified by the effect of atmospheric warming,
758 similarly to the conclusions drawn from our EXP4 results.

759



760

761 **Figure 1412:** Multi-model mean of the ice thickness loss compared to the initial ice sheet for different basal
 762 melting perturbations. LGM ice sheets are built by fixing the basal melting to 0.1 m yr^{-1} (as in Petrini et al., 2020;
 763 Alvarez-Solas et al., 2019). Note that the significant decrease in ice thickness in the Norwegian and Greenland
 764 seas is due to the simulation of ice shelves in the new spin-up for the MIROC-ESM forcing (see Fig. SP12SP13).
 765 These ice shelves are extremely sensitive to a change in the basal melt. The white line indicates the areas where
 766 the multi-model mean is done on the 5 models.

767 The second round of sensitivity experiments conducted with new values of climate-related parameters and new
 768 parameterizations related to the ice dynamics also confirm the high sensitivity of the EIS to the atmospheric forcing
 769 in the GRISLI ice sheet model. This contrasts with the current situation in the West Antarctic Ice Sheet (WAIS),
 770 where ice volume loss is mainly due to melting under the ice shelves (Pritchard et al., 2012). This difference in the
 771 response of the two ice sheets raises questions about the mechanisms responsible for their respective evolution.

772 In addition, WAIS is characterized by large areas of confined ice shelves exerting a buttressing effect on the
 773 grounded ice, whereas most of the ice shelves in our simulated LGM EIS are unconfined (see Section 4.4.2)
 774 However, as temperatures are expected to rise in the future, larger amounts of meltwater will be produced on the
 775 surface of the ice shelves (Kittel et al., 2021), favouring potentially the ice-shelf disintegration through
 776 hydrofracturing (Banwell et al., 2013; Lai et al., 2020). Although this process differs from basal melting, it could
 777 bring WAIS into a similar configuration to the past Eurasian ice sheet.

778 The ISMIP6 project (Seroussi et al., 2020) shows a significant difference in ice sheet behavior depending on the
 779 ice sheet model used (Seroussi et al., 2020). Despite the numerous sensitivity experiments presented in this study
 780 with various parameter values and different parameterizations of the ice dynamics (see section 4.4), we cannot
 781 totally exclude the possible model-dependency of our results To reduce the uncertainties associated with the use
 782 of a single ice sheet model, we strongly encourage other ice-sheet modelers to perform the same kind of sensitivity
 783 tests with several other ice sheet models having, if possible, higher resolution so as to better capture the fine-scale
 784 structure of outlet glaciers and the ice flow dynamics at the grounding line and the marine ice sheet instability.

785 6. Conclusion

786 In this paper, we used off-line GRISLI2.0 simulations forced by PMIP3/PMIP4 models to investigate the key
 787 mechanisms driving the retreat of the Eurasian ice complex at the beginning of the last deglaciation. We gave a
 788 special attention to the understanding of the processes responsible for the destabilization of the marine-based parts
 789 of the Eurasian ice sheets as GRISLI2.0 includes an explicit calculation of the ice flux at the grounding line which
 790 is expected to account for the representation of the marine ice sheet instability. We first showed that, due to too

791 strong climate biases in some GCMs at the LGM, only 5 out of 10 GCMs succeeded in building an ice sheet in
792 agreement with the reconstructions.

793 The sensitivity experiments have been designed to test the response of the simulated Eurasian ice sheets to surface
794 climate, oceanic temperature and sea level perturbations. Our results highlight the high EIS sensitivity to a change
795 in surface atmospheric temperatures- using the GRISLI model. While basal melting does not seem to be the main
796 driver of the ice sheet retreat, we showed that its effect is clearly amplified by the atmospheric warming.

797 These results contradict those of previous studies mentioning the central role of the ocean on the deglaciation of
798 BKIS. However, we argue that parts of this disagreement are related to the way the climatic forcing is done
799 (absolute climatic fields, anomalies or climatic indexes) and the procedure followed for building the initial state
800 of EIS and to the presence of confined or unconfined ice shelves at the LGM. In order to assess the robustness of
801 our analyses, we suggest to other modelling groups to reproduce the same kind of sensitivity tests with ice sheet
802 models of similar or higher complexity. This pluralistic approach would allow to better understand the
803 uncertainties associated with the ice sheet model used.

804 ~~This study highlights several differences regarding the respective behaviors of the Eurasian ice sheet during the~~
805 ~~last deglaciation and the present day West Antarctic ice sheet. While EIS appears primarily sensitive to the~~
806 ~~atmospheric forcing, WAIS is mainly driven by dynamic ice discharges triggered by the ocean warming. In~~
807 ~~addition, WAIS is characterized by large areas of confined ice shelves exerting a buttressing effect on the grounded~~
808 ~~ice whereas most of the ice shelves in our simulated LGM EIS are unconfined. However, as temperatures~~
809 ~~rise in the future, larger amounts of meltwater will be produced on the surface of the ice shelves (Kittel et al.,~~
810 ~~2021), favouring potentially the ice shelf disintegration through hydrofracturing (Banwell et al., 2013; Lai et al.,~~
811 ~~2020). Although, this process differs from basal melting, it could bring WAIS into a similar configuration to the~~
812 ~~past Eurasian ice sheet.~~

813 **Data availability.** The source data of the experiments presented in the main text of the paper are available on the
814 Zenodo repository with the digital object identifier <https://doi.org/10.5281/zenodo.7528183> (van Aalderen et al,
815 2023).

816 **Code availability.** The GRISLI2.0 code is available upon request from Aurelien Quiquet
817 (aurelien.quiquet@lsce.ipsl.fr) and Christophe Dumas (christophe.dumas@lsce.ipsl.fr) (Laboratoire des Sciences
818 du Climat et de l'Environnement (LSCE)).

819 **Author contributions.** All authors designed the study. VVA performed the numerical experiments. All authors
820 contributed to the analysis of model results. VVA and SC wrote the manuscript with inputs from CD and AQ.

821 **Competing interests.** The authors declare that they have no conflict of interest

822 **Acknowledgements.** The authors are very grateful to Irina Rogozhina who edited the manuscript as well as two
823 anonymous reviewers for their constructive comments that greatly help improve the manuscript. Victor van
824 Aalderen is funded by the French National Research Agency (Grant: ANR-19-CE01-15). We acknowledge the
825 World Climate Research Programme's Working Group on Coupled Modelling, which is responsible for the
826 Paleoclimate Modelling Intercomparison Project (PMIP) and we thank the climate modeling groups (listed in

827 Table 1 of this paper) for producing and making available their model ~~output~~outputs. This work benefited from
828 productive exchanges with ~~N. Jourdain~~Nicolas Jourdain and ~~D. Didier~~ Swingedouw.

829

830

831

832

833

834

835

836

837

838

839

840

841